

On the Relation between the Inclination Angle of the Accretion Disk and the Broad-line Region in Active Galactic Nuclei

RONG DU ^{1,2} LUIS C. HO ^{1,2} YUANZE DING ³ AND RUANCUN LI ^{1,2}

¹*Department of Astronomy, School of Physics, Peking University, Beijing 100871, China*

²*Kavli Institute for Astronomy and Astrophysics, Peking University, Beijing 100871, China*

³*Division of Physics, Mathematics and Astronomy, California Institute of Technology, Pasadena, CA 91125, USA*

ABSTRACT

Models of active galactic nuclei often invoke a close physical association between the broad-line region and the accretion disk. We evaluate this theoretical expectation by investigating the relationship between the inclination angle of the BLR (θ_{BLR}) and the inclination angle of the inner accretion disk (θ_{disk}). For a sample of eight active galactic nuclei that have published values of θ_{BLR} estimated from dynamical modeling of the BLR based on velocity-resolved reverberation mapping experiments, we analyze high-quality, joint XMM-Newton and NuSTAR X-ray observations to derive new, robust measurements of θ_{disk} through broadband (0.3–78 keV) reflection spectroscopy. We find a strong, positive correlation between θ_{BLR} and θ_{disk} (Pearson correlation coefficient 0.856, p -value 0.007), although Monte Carlo simulations indicate that the level of significance is only marginal ($< 3\sigma$). Nevertheless, the nearly linear relation between θ_{BLR} and θ_{disk} suggests of a possible physical alignment between the accretion disk and the BLR. Future studies with a larger and more homogeneous sample are needed to confirm the correlation and refine our understanding of the structure and dynamics of the central regions of active galaxies.

Keywords: Accretion (14), Active galaxies (17), Seyfert galaxies(1447), Reverberation mapping(2019), X-ray active galactic nuclei (2035), Supermassive black holes (1663)

1. INTRODUCTION

Active galactic nuclei (AGNs) are characterized by the accretion of matter onto their central supermassive black hole (BH) at sub-pc scales, where complex dynamics and multiple physical structures coexist, including the accretion disk and the broad-line region (BLR). The strong broad emission lines arise from BLR gas largely photoionized by intense ultraviolet (UV) to X-ray radiation from the accretion disk (e.g., Krolik 1998). Various attempts have been made to model the BLR in the context of accretion disk winds. Emmering et al. (1992) proposed that clouds in a centrifugally driven magnetohydrodynamic wind extract angular momentum from the accretion disk and are photoionized by the UV radiation from the inner accretion disk. Murray & Chiang (1995) and Murray et al. (1995) suggested that the

BLR is produced by a smooth, nonspherical disk wind driven by UV emission lines and gas pressure. By contrast, the failed dusty outflow model (e.g., Czerny & Hryniewicz 2011; Czerny et al. 2017; Baskin & Laor 2018; Pandey et al. 2023) claims that the BLR originates from a dust wind in the atmosphere of the disk powered by local radiation pressure; once lifted above the disk, the dust evaporates due to the central emission of the AGN, leading to subsequent fallback of the wind toward the disk. The quasar rain model (Elvis 2000, 2017), on the other hand, argues that the BLR arises from a condensed warm disk wind driven by varying radiation pressure, and that, once formed, such clouds rain back down toward the BH and then are destroyed by the warm absorbers (WAs; Halpern 1984; Reynolds 1997). The disappearance of broad emission lines at very low luminosities (Ho 2008) finds a natural explanation in the context of disk wind model for the origin of the BLR (e.g., Czerny et al. 2004; Elitzur & Ho 2009; Elitzur et al. 2014).

A common feature shared qualitatively among all these models is that BLR has an axisymmetric geometry with an opening angle and an inclination angle, representing the poloidal average of the spatial configuration of the system. The inclination angle of the BLR to the line-of-sight (θ_{BLR}) should be roughly similar to the inclination of the disk (θ_{disk}). To date, however, this basic prediction has yet to be verified, owing to the observational challenge of constraining the sub-structures of AGNs on such small scales.

Spatially resolving the BLR remains out of reach except for a handful of the brightest AGNs amenable to near-infrared interferometry (e.g., [GRAVITY Collaboration et al. 2018](#)). Under most circumstances, the kinematics and structure of the BLR can only be probed indirectly through reverberation mapping (RM; [Bahcall et al. 1972](#); [Blandford & McKee 1982](#)), by measuring the time delay between the variations in accretion disk emission and the corresponding changes in the broad emission lines. However, it is nontrivial to interpret the complex information encoded in the RM transfer function ([Horne 1994](#); [Skjelboe et al. 2015](#)). Parameterized phenomenological models ([Brewer et al. 2011](#); [Pancoast et al. 2011, 2012, 2014a](#); [Li et al. 2013](#)) have been applied successfully to numerous RM campaigns to extract physical properties of the BLR (e.g., [Bentz et al. 2009](#); [Denney et al. 2009, 2010](#); [Barth et al. 2011a,b](#); [Grier et al. 2013](#); [Du et al. 2016, 2018](#); [Pei et al. 2017](#); [De Rosa et al. 2018](#); [Feng et al. 2021](#); [Li et al. 2021](#)). Such dynamical modeling of velocity-resolved RM data depicts the BLR as an axisymmetric thick geometry with low to moderate θ_{BLR} , whose kinematics are largely governed by a combination of Keplerian rotation and some degree of radial motions (e.g., [Pancoast et al. 2014b](#); [Grier et al. 2017](#); [Li et al. 2018](#); [Williams et al. 2018, 2020](#); [Bentz et al. 2021](#); [Villafañã et al. 2022](#)).

Probing structures on the scale of the accretion disk presents even more formidable challenges. Fitting broadened emission lines with a relativistic accretion disk model ([Novikov & Thorne 1973](#); [Shakura & Sunyaev 1973](#)), we can measure θ_{disk} using the double-peaked broad $\text{H}\alpha$ emission line (e.g., [Eracleous & Halpern 1994](#); [Storchi-Bergmann et al. 1997](#); [Ho et al. 2000](#)) or the broad $\text{Fe K}\alpha$ 6.4 keV line when a specific corona configuration is assumed (e.g., [Nandra et al. 1997](#)). Indirect inferences on θ_{disk} can also be made, for instance by assuming that the disk is normal to the jet and estimating the jet orientation from the core dominance of radio-loud sources (e.g., [Ghisellini et al. 1993](#); [Wills & Brotherton 1995](#)). In the context of the AGN unified model ([Antonucci 1993](#)), one can attempt a first-order approximation of θ_{disk} by mapping the dy-

namics of the narrow-line region ([Fischer et al. 2013](#)), or by modeling the infrared spectral energy distribution to constrain the inclination angle of the dusty torus ([Zhuang et al. 2018](#)).

[Du et al. \(2024\)](#) recently tested the methodology to measure the inclination angle of the inner accretion disk through X-ray reflection spectroscopy. The X-ray emission in AGNs is explained conventionally by hot coronal electrons near the BH inverse-Comptonizing thermal optical or UV photons from the accretion disk into an exponential cutoff power-law continuum (e.g., [Haardt & Maraschi 1991](#)). Two reflection components often overlie on the power-law continuum: the $\text{Fe K}\alpha$ fluorescence line at 6 – 7 keV ([Fabian et al. 1989](#)) and the Compton scattering hump of the continuum emission peaking at 20 – 40 keV ([Guilbert & Rees 1988](#)). The corona irradiates the inner disk region, where gravitational redshift, relativistic beaming, and the Doppler effect broaden the $\text{Fe K}\alpha$ line by stretching the low-energy wing and creating a sharper blueshifted peak. The line broadening effects encode information on the velocity of the emitting fluid element as a function of disk inclination and the radius of the emitters, and we can infer θ_{disk} by fitting a broadband spectrum with a numerical reflection model. Advanced models have been developed for calculating a relativistically blurred, broadband reflection continuum, including the KY package ([Dovčiak et al. 2004](#)), REFLKERR ([Niedźwiecki et al. 2019](#)), RELTRANS ([Ingram et al. 2019](#)), and RELXILL ([Dauser et al. 2014](#); [García et al. 2014](#)). For our purposes, we adopt the self-consistent, angle-dependent reflection model RELXILL.

Much of the recent interest in BLR modeling is motivated by the desire to measure BH masses in AGNs. So-called single-epoch virial mass estimates of the BH (e.g., [Vestergaard & Peterson 2006](#); [Ho & Kim 2015](#)) depend linearly on a scale factor f_{BLR} , which accounts for the detailed structure, dynamics, and orientation of the BLR. The unknown geometry and inclination angle of the BLR, in particular, lead to larger uncertainties in the M_{BH} estimation ([Krolik 2001](#)). While dynamical modeling offers an avenue to estimate θ_{BLR} , how can we test the reliability of these results? Verifying that $\theta_{\text{BLR}} \approx \theta_{\text{disk}}$ would lend confidence that the BLR inclinations are not too far off the mark. Moreover, a close association between θ_{BLR} and θ_{disk} would also help validate theoretical models that associate the BLR clouds with material in the accretion disk or closely aligned with it. Of course, θ_{BLR} may not align perfectly with θ_{disk} . Radiation pressure, magnetic fields, and turbulence can break the symmetry of the system and cause the BLR to be tilted or warped relative to the accretion

disk. For instance, the BLR can assume a more spherical distribution in the above-mentioned wind models (e.g., [Emmering et al. 1992](#); [Czerny et al. 2016](#)), potentially offering insights on AGN feeding and feedback processes. Additional substructures or dynamical interactions in the AGN environment may further complicate any simple expectations of co-planarity between the BLR and the accretion disk.

We aim to study the inclination angles in AGNs, exploring the connection between the accretion disk and other facets of the AGN and its host galaxy. We investigate the possible correlation between the inclination angle of the BLR and the inclination angle of the inner accretion disk in a small sample of nearby AGNs that have both θ_{BLR} measurements secured from published RM dynamical modeling and θ_{disk} derived in this study through X-ray reflection spectroscopy. We adopt a cosmology with $H_0 = 70 \text{ km s}^{-1} \text{ Mpc}^{-1}$, $\Omega_\Lambda = 0.73$, and $\Omega_m = 0.27$.

2. EXPERIMENTAL DESIGN AND METHODOLOGY

2.1. Sample Definition

Our objective is to derive θ_{disk} measurements for AGNs that already have published values of θ_{BLR} . To this end, we start by assembling all type 1 (broad-line) AGNs with high-quality RM observations for which phenomenological dynamical models of the BLR have been constructed using the Code for AGN Reverberation and Modeling of Emission Lines (CARAMEL) developed by [Pancoast et al. \(2011, 2014a\)](#). The model has been applied systematically to 28 AGNs with velocity-resolved RM data of the $\text{H}\beta$ emission line ([Pancoast et al. 2014b](#); [Grier et al. 2017](#); [Williams et al. 2018, 2020](#); [Bentz et al. 2021, 2022](#); [Villafaña et al. 2022, 2023](#)). These form our primary sample.

Additionally, we acknowledge the Bayesian estimator developed by [Li et al. \(2013, 2018\)](#), which constrains the size and structure of the BLR through dynamical modeling based on [Pancoast et al. \(2011\)](#). This method incorporates the nonlinear emission response of the BLR to continuum variations and has been successfully applied to several AGNs (e.g., [Du et al. 2014, 2015, 2016, 2018](#); [Wang et al. 2014](#); [Li et al. 2018](#); [Xiao et al. 2018](#); [Lu et al. 2019](#)). However, we choose not to include results from this approach in the present study to avoid potential inconsistencies arising from different BLR modeling techniques. Moreover, most AGNs in their sample are super-Eddington sources, which do not overlap with our primary sample. These sources may also introduce conflicts with our X-ray reflection modeling, which is based on the assumption of a standard accretion disk.

For our purpose, the X-ray observations must satisfy a number of requirements in order to obtain reliable measurements of θ_{disk} . Guided by the tests presented in [Du et al. \(2024\)](#), we search for multi-epoch, high-quality X-ray data from the public data archives of the X-ray Multi-Mirror Mission (XMM-Newton; [Jansen et al. 2001](#), 0.3–10 keV) and the Nuclear Spectroscopy Telescope Array (NuSTAR; [Harrison et al. 2013](#), 3–78 keV). We favor sources with simple absorbing features to reduce the complexity of the spectral fitting and to minimize the uncertainties in θ_{disk} caused by this contaminant. From the original sample of 28 AGNs with RM-based measurements of θ_{BLR} , only eight sources remain that have clearly measured reflection components yet with simply modeled WAs. Table 1 summarizes the X-ray observations of the final sample, among which [Williams et al. \(2018\)](#) analyzed Mrk 279, Mrk 50, PG 1310–108, and Zw 229–015 as part of the Lick AGN Monitoring Project (LAMP) 2011 ([Barth et al. 2015](#)) and [Villafaña et al. \(2022\)](#) analyzed MCG +04–22–042, Mrk 1392, PG 2209+184, and RBS 1917 in connection with the LAMP 2016 program ([U et al. 2022](#)).

2.2. Derivation of Accretion Disk Inclination

The inner accretion disk inclination, formally defined as the viewing angle with respect to its norm, is measured by jointly fitting the broadband X-ray spectra of AGNs using the self-consistent, angle-dependent reflection model RELXILL ([Dauser et al. 2014](#); [García et al. 2014](#)). This model solves for the inclination θ_{disk} , dimensionless spin parameter a_* , iron abundance A_{Fe} , power-law photon index Γ , ionization state ξ , electron temperature kT_e , reflection fraction R_f , and coronal emissivity parameters Index_1 and Index_2 , and the broken radius R_{br} . Specifically, we use RELXILLCP in the RELXILL family to account for the soft excess, broad Fe line, and Compton hump (see Section 5.6 of [Du et al. 2024](#)).

We use spectra retrieved from the PN charge-coupled device and Metal Oxide Semiconductor (MOS) of the European Photon Imaging Camera (EPIC) onboard XMM-Newton, and from the two focal plane modules (FPMA/B) of NuSTAR. We select the 0.3–10 keV band for XMM-Newton and the 3–78 keV band for NuSTAR, ignoring all bad spectral bins. We divide observations chronologically into different epochs for each source and fit the epochs jointly. Spectral fittings are conducted using XSPEC (12.12.1; [Arnaud 1996](#)) with the modified [Levenberg \(1944\)–Marquardt \(1963\)](#) algorithm to minimize the χ^2 statistic ([Bevington 1969](#)), and posterior parameter distributions are generated to determine confidence intervals.

Table 1. Summary of X-ray Observations

Name	Redshift ^a	Epoch	Observatory	Observation ID	Effective Exposure (ks)
(1)	(2)	(3)	(4)	(5)	(6)
MCG +04−22−042	0.03311	<i>a</i>	XMM-Newton	0312191401	1.4 (PN) / 9.2 (MOS)
		<i>b</i>	NuSTAR	60061092002	18.8
		<i>c</i>	NuSTAR	60602018002	43.0
		<i>d</i>	NuSTAR	60602018004	42.6
		<i>e</i>	NuSTAR	60602018006	40.7
Mrk 50	0.02386	<i>a</i>	XMM-Newton	0650590401	11.7
		<i>b</i>	NuSTAR	60061227002	17.4
Mrk 279	0.03045	<i>a</i>	XMM-Newton	0872391301	20.0
		<i>b</i>	NuSTAR	60601011004	200.6
Mrk 1392	0.03588	<i>a</i>	XMM-Newton	0795670101	25.6
		<i>b</i>	NuSTAR	60160605002	21.1
PG 1310−108	0.03427	<i>a</i>	XMM-Newton	0801891601	19.4
PG 2209+184	0.06990	<i>a</i>	XMM-Newton	0795620201	36.2
			NuSTAR	60301015002	101.9
RBS 1917	0.06600	<i>a</i>	XMM-Newton	0762871101	33.6
Zw 229−015	0.02788	<i>a</i>	XMM-Newton	0672530301	27.5
		<i>b</i>	NuSTAR	60160705002	22.0

^aRedshift obtained from the NASA/IPAC Extragalactic Database (NED).

2.3. Observations and Data Reduction

Data from both XMM-Newton and NuSTAR for the eight sources in our sample are gathered and processed to retrieve the spectra. We divide the spectra of each source into different epochs according to the observed date and respective instrument (Table 1). For XMM-Newton data, light curves and spectra are extracted from EPIC detectors using System Analysis Software (version 20.0.0; calibration files version 31 of March 2022). Event lists are retrieved using the tasks **epproc** and **emproc**, source and background spectra are extracted with **evselect**, and ancillary files and redistribution matrices are generated with **arfgen** and **rmfgen**. In the absence of pile-up, source spectra are extracted from a 40''-diameter circular region. For Mrk 50, corrections for pile-up are made using an annulus region between 10'' and 30'' in diameter. Background spectra are extracted from source-free polygon regions for PN observations and a 300''-diameter circular region for MOS observations. Spectra are rebinned with **specgroup** to have at least 25 counts per bin and not oversample the full width at half-maximum resolution by more than a factor of 3. For NuSTAR data, event lists from both FPM detectors are retrieved with **NUPIPELINE** in NUS-

TARDAS (2.1.2; calibration files from CALDB version 20220802) within the HEASOFT bundle (6.30.1). With **NUPRODUCTS**, spectra are extracted from a 40''-diameter circular region centered on the source, with background spectra from a source-free 300''-diameter circle near the source. Spectra are rebinned with **ftgroupppha** to have at least 25 counts per bin.

2.4. Spectral Fitting

We analyze the sources with a baseline model that takes into consideration Galactic absorption, blackbody emission, the reflection continuum, and WAs¹. For each source, we initially fit a phenomenological redshifted power-law model (ZPOWERLW) modified by Galactic absorption (TBABS; see Wilms et al. 2000). Broadband fitting with systematic residuals at soft and hard energies motivate using RELXILLCP to model the soft excess, the broad Fe K α line, and the high-energy Compton hump. As in Du et al. 2024 (see their Section 5.7), we also model the mild soft excess with an additional epoch-independent redshifted blackbody (ZBBODY) component. WAs in the soft

¹ In XSPEC terminology:

CONSTANT*TBABS*XSTAR*(ZBBODY+RELXILLCP).

band are fit with multiplicative XSTAR tables, with three free parameters per XMM-Newton epoch: hydrogen column density N_{H} , ionization parameter ξ_{WA} , and outflow velocity v . The XSTAR tables are generated with an input power-law continuum with photon index $\Gamma = \{1.0, 3.0, 5.0, \dots, 15.0\} \times 10^{-1}$, turbulent velocity 500 km s^{-1} , $\log(N_{\text{H}}/\text{cm}^{-2}) = \{19.0, 19.5, 20.0, 20.5, \dots, 23.0\}$, and $\log(\xi_{\text{WA}}/\text{erg cm s}^{-1}) = \{-2.0, -2.0 + 5/9, -2.0 + 2 \times 5/9, \dots, 3.0\}$. Although multi-phase WAs or ultra-fast outflows are likely to exist in some sources, it is beyond the scope of our analysis to deal with the complicated soft-band emission, absorption, and reprocessing features, which, in any case, would require higher resolution soft X-ray spectra, such as those from the Reflection Grating Spectrometer (RGS; [den Herder et al. 2001](#)). One XSTAR table is usually sufficient in this work.

During the fit, the Galactic absorption column density is fixed to values from the Leiden/Argentine/Bonn Galactic HI Survey ([Kalberla et al. 2005](#)). The black-body temperature kT is a free parameter but assumed constant across spectral epochs. For RELXILLCP, disk-related parameters (θ_{disk} , a_* , and A_{Fe}) are fixed across all epochs, while corona-related parameters (Γ , kT_e , R_f , Index_1 , Index_2 , R_{br} , and ξ) are free between different epochs. Inner radius (R_{in} = radius of the innermost stable circular orbit), outer radius ($R_{\text{out}} = 400r_g$, where $r_g := GM/c^2$), and density ($n = 10^{15} \text{ cm}^{-3}$) are fixed. Cross-calibration constants account for instrument differences, and normalization parameters compensate for variations in integrated flux and exposure time.

Upon achieving the best fit, we use a Markov chain Monte Carlo (MCMC; [Metropolis et al. 1953](#)) algorithm to generate the posterior probability distributions of the baseline parameters. We use the [Goodman & Weare \(2010\)](#) algorithm with 200 walkers, generating proposals from a Gaussian distribution around the best-fit values. Chain convergence is tested with integrated autocorrelation time τ_f using EMCEE ([Foreman-Mackey et al. 2013](#)), with reference to the evolution history of the model parameters and fit statistics. Chains run longer than $\sim 1000 \tau_f$ ([Sokal 1996](#)), with a 10% burn-in rejection of initial chain elements. We calculate the 90% confidence intervals of all parameters from the MCMC chains.

Table 2 gives an overview of the best-fit values of the continuum. We summarize the best-fit values of the accretion disk inclination, the BLR inclination, together with the galactic disk inclination (see Section 3.6) in Table 3. In Appendix A, we provide details of the spec-

tral fitting for each source, and the results for the WAs are concluded in Table A1.

Table 2. Best-fit Parameters for the X-ray Continuum

Name	Epoch	θ_{disk} ($^{\circ}$)	a_*	A_{Fe} (A_{\odot})	R_f	kT_e (keV)	Γ	Index ₁	Index ₂	R_{br} (r_g)	$\log \xi$ (erg cm s $^{-1}$)	$L_{0.1-200 \text{ keV}}$ (10^{44} erg s $^{-1}$)
(1)	(2)	(3)	(4)	(5)	(6)	(7)	(8)	(9)	(10)	(11)	(12)	(13)
MCG+04-22-042	<i>a</i>				$2.82^{+0.50}_{-0.32}$	91^{+15}_{-23}	1.91 ± 0.04	$8.2^{+0.4}_{-0.3}$	$1.5^{+0.3}_{-0.2}$	$7.7^{+1.1}_{-1.0}$	$2.87^{+0.13}_{-0.19}$	0.90 ± 0.02
	<i>b</i>				$0.32^{+0.11}_{-0.12}$	72^{+10}_{-11}	$1.84^{+0.05}_{-0.04}$	$9.0^{+0.8}_{-1.1}$	2.2 ± 0.4	$3.0^{+0.9}_{-0.8}$	$2.96^{+0.08}_{-0.18}$	2.36 ± 0.11
	<i>c</i>	$15.2^{+2.2}_{-1.5}$	$0.996^{+0.002}_{-0.013}$	> 8.0	$0.97^{+0.18}_{-0.15}$	20 ± 4	1.82 ± 0.04	$8.8^{+0.5}_{-0.5}$	$2.5^{+0.3}_{-0.2}$	$3.1^{+0.4}_{-0.4}$	$2.45^{+0.36}_{-0.59}$	1.82 ± 0.06
	<i>d</i>				$0.73^{+0.14}_{-0.28}$	74^{+11}_{-18}	1.87 ± 0.04	8.6 ± 1.1	$1.6^{+0.2}_{-0.4}$	$4.9^{+1.1}_{-0.6}$	$2.76^{+0.19}_{-0.29}$	1.93 ± 0.06
	<i>e</i>				$1.15^{+0.29}_{-0.31}$	> 400	$1.83^{+0.07}_{-0.10}$	$8.9^{+0.9}_{-1.5}$	2.3 ± 0.2	$3.6^{+0.6}_{-0.4}$	$3.01^{+0.31}_{-0.56}$	1.12 ± 0.05
Mrk 50	<i>a</i>	$19.1^{+2.0}_{-3.3}$	$0.992^{+0.005}_{-0.030}$	$3.5^{+0.4}_{-0.2}$	$2.84^{+0.37}_{-0.42}$	> 400	$1.75^{+0.05}_{-0.06}$	> 9.5	$4.3^{+0.4}_{-0.5}$	$2.4^{+0.3}_{-0.2}$	$3.24^{+0.06}_{-0.08}$	0.22 ± 0.01
	<i>b</i>				$0.59^{+0.09}_{-0.12}$	24^{+4}_{-3}	$1.76^{+0.07}_{-0.05}$	$2.5^{+0.4}_{-0.6}$	$7.8^{+1.0}_{-2.1}$	$20.1^{+2.5}_{-2.9}$	$3.13^{+0.24}_{-0.27}$	0.45 ± 0.04
Mrk 279	<i>a</i>	$26.9^{+2.5}_{-3.7}$	$0.997^{+0.001}_{-0.006}$	$6.3^{+2.4}_{-1.5}$	$0.57^{+0.66}_{-0.24}$	20^{+10}_{-9}	1.86 ± 0.01	> 7.3	$2.3^{+0.1}_{-0.2}$	$3.1^{+0.4}_{-0.2}$	$3.14^{+0.08}_{-0.10}$	1.13 ± 0.01
	<i>b</i>				$1.90^{+1.00}_{-0.73}$	42^{+18}_{-14}	$1.81^{+0.07}_{-0.04}$	> 8.9	$1.0^{+0.5}_{-0.6}$	$5.1^{+1.3}_{-0.8}$	$1.48^{+0.39}_{-0.57}$	0.68 ± 0.01
Mrk 1392	<i>a</i>	$25.5^{+6.7}_{-9.9}$	$0.942^{+0.038}_{-0.093}$	$0.51^{+0.07}_{-0.01}$	> 7.36	257^{+124}_{-110}	2.05 ± 0.07	$6.9^{+1.7}_{-1.1}$	3.2 ± 0.7	$4.7^{+2.3}_{-1.1}$	$2.46^{+0.20}_{-0.22}$	0.53 ± 0.01
	<i>b</i>				$4.78^{+2.11}_{-1.63}$	170^{+100}_{-98}	$1.82^{+0.10}_{-0.09}$	$6.7^{+2.5}_{-3.0}$	$1.4^{+0.8}_{-1.2}$	$4.8^{+2.2}_{-1.7}$	$3.26^{+0.33}_{-0.18}$	0.72 ± 0.06
PG 1310-108	<i>a</i>	$33.5^{+20.8}_{-22.4}$	$0.903^{+0.091}_{-0.403}$	$4.7^{+1.6}_{-1.5}$	< 2.02	23^{+35}_{-12}	$1.90^{+0.03}_{-0.09}$	$4.4^{+2.7}_{-3.4}$	< 4.4	39^{+75}_{-31}	$3.01^{+0.58}_{-0.13}$	0.47 ± 0.01
PG 2209+184	<i>a</i>	$35.6^{+31.7}_{-25.9}$	$0.989^{+0.009}_{-0.079}$	$4.7^{+1.6}_{-1.4}$	$0.42^{+0.29}_{-0.21}$	89^{+55}_{-40}	1.90 ± 0.02	$6.6^{+2.6}_{-3.7}$	$2.1^{+0.8}_{-1.6}$	$5.1^{+2.6}_{-2.3}$	$2.92^{+0.11}_{-0.15}$	1.78 ± 0.01
RBS 1917	<i>a</i>	$17.2^{+4.5}_{-1.1}$	$0.977^{+0.012}_{-0.003}$	$4.1^{+0.1}_{-0.1}$	> 9.87	> 380	$2.11^{+0.07}_{-0.02}$	> 8.6	3.1 ± 0.1	$4.5^{+0.2}_{-0.7}$	$2.68^{+0.04}_{-0.18}$	1.63 ± 0.02
Zw 229-015	<i>a</i>	$26.2^{+2.5}_{-0.5}$	$0.993^{+0.005}_{-0.059}$	$6.3^{+0.4}_{-0.1}$	$0.50^{+0.10}_{-0.03}$	52^{+32}_{-7}	$1.78^{+0.01}_{-0.02}$	$6.5^{+0.5}_{-0.1}$	$7.8^{+0.1}_{-0.3}$	< 1.1	2.87 ± 0.01	0.18 ± 0.01
	<i>b</i>				$1.38^{+0.27}_{-0.06}$	14^{+2}_{-1}	$1.80^{+0.10}_{-0.01}$	$3.6^{+0.1}_{-0.1}$	$8.9^{+0.1}_{-0.5}$	$2.1^{+0.4}_{-0.1}$	$1.55^{+0.02}_{-0.12}$	0.40 ± 0.03

NOTE— Col. (1): Name of the source. Col. (2): Epoch. Col. (3): Inclination angle of the accretion disk. Col. (4): Dimensionless BH spin. Col. (5): Iron abundance in units of the solar abundance. Col. (6): Reflection fraction. Col. (7): Temperature of the corona. Col. (8): Photon index. Col. (9): Power-law index 1 for the broken power-law disk emissivity. Col. (10): Power-law index 2 for the broken power-law disk emissivity. Col. (11): Break radius for the broken power-law disk emissivity, in units of the gravitational radius $r_g = GM/c^2$. Col. (12): Ionization parameter of the accretion disk. Col. (13): Luminosity in the 0.1–200 keV band of the power-law continuum. For sources observed in more than one epoch, the spin, inclination, and iron abundance are fit simultaneously for all epochs. The best-fit values and 90% confidence intervals are presented.

Table 3. Key Angles of the Eight Sources

Name	θ_{disk}	θ_{BLR}	θ_o	q	θ_{gal}
	($^\circ$)	($^\circ$)	($^\circ$)		($^\circ$)
(1)	(2)	(3)	(4)	(5)	(6)
MCG +04–22–042	$15.2^{+2.2}_{-1.5}$	$11.3^{+5.8}_{-5.0}$	$13.6^{+6.9}_{-4.9}$	0.56	57.7
Mrk 50	$19.1^{+2.0}_{-3.3}$	$19.8^{+6.0}_{-5.4}$	$14.1^{+4.8}_{-3.7}$	0.72	45.1
Mrk 279	$26.9^{+2.5}_{-3.7}$	$29.1^{+3.4}_{-3.4}$	$41.0^{+4.3}_{-4.1}$	0.70	46.8
Mrk 1392	$25.5^{+6.7}_{-9.9}$	$25.5^{+3.4}_{-2.8}$	$41.2^{+5.3}_{-4.8}$	0.50	62.1
PG 1310–108	$33.5^{+20.8}_{-22.4}$	$44.0^{+35.0}_{-13.0}$	$58.0^{+25.0}_{-16.0}$	0.86	31.4
PG 2209+184	$35.6^{+31.7}_{-25.9}$	$30.2^{+8.7}_{-6.9}$	$29.1^{+11.0}_{-8.4}$	0.84	33.6
RBS 1917	$17.2^{+4.5}_{-1.1}$	$20.2^{+9.9}_{-3.9}$	$25.1^{+9.2}_{-7.5}$	0.70	46.8
Zw 229–015	$26.2^{+2.5}_{-0.5}$	$32.9^{+6.1}_{-5.2}$	$33.5^{+6.4}_{-6.2}$	0.56	57.7

NOTE— Col. (1): Name of the source. Col. (2): Inclination angle of the inner accretion disk with 90% confidence intervals from our X-ray reflection spectroscopy as detailed in Appendix A. Col. (3): Inclination angle of the BLR with 68% confidence intervals collected from Williams et al. (2018) and Villafañá et al. (2022). Col. (4): Opening angle of the BLR with 68% confidence intervals also collected from both works. Col. (5): Axial ratio $q = b/a$ in the 2MASS K_s band from Jarrett et al. (2000). Col. (6): Inclination angle of the galactic disk.

3. RESULTS AND DISCUSSION

3.1. Correlation Analysis

We plot the inclinations of the BLR against those of the inner accretion disk in Figure 1. The standard Pearson correlation coefficient between the two inclinations is 0.856, and a T -test with null hypothesis of no correlation returns a p -value of 0.007. Therefore, we have $\sim 99\%$ confidence ($\sim 2.72\sigma$) that a strong positive relationship exists. We run Monte Carlo simulations to determine the probability that such a one-to-one correlation might arise from an actual underlying relation given the errors of the inclination measurements. We generate random data points for both inclinations with Gaussian distributions of the measured values and their errors, and calculate the correlation coefficient and p -value for each simulation. From 10^3 to 10^6 realizations, the probability of obtaining a p -value less than 0.05 is 39%, and the probability of obtaining a p -value less than 0.01 converges to $\sim 15\%$, with a mean correlation coefficient of 0.56. The significance levels for both the existence and absence of a genuine correlation are at a subtle level of $< 3\sigma$. Considering the empirically derived errors of both variables, a Deming (1943) regression gives

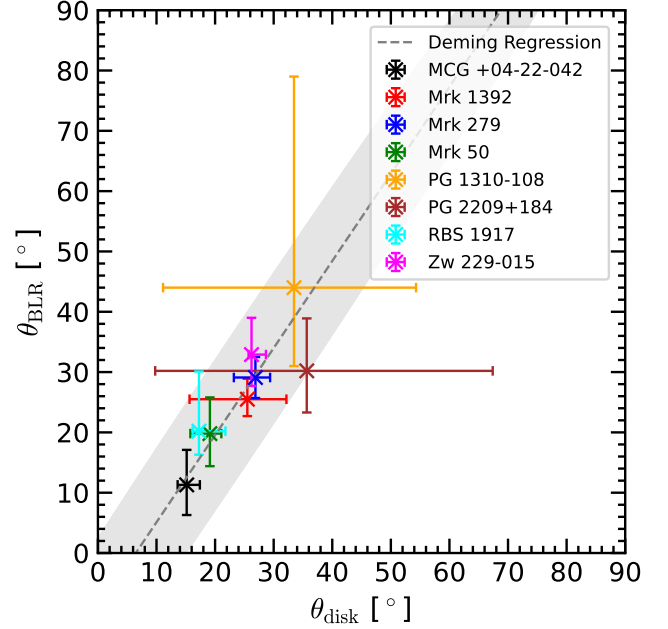


Figure 1. The relation between the BLR inclination versus the inner accretion disk inclination. The gray dashed line depicts the relation obtained from the Deming regression. The gray shaded region represents the 90% confidence band of the regression.

$$\theta_{\text{BLR}} = (1.444 \pm 0.648) \times \theta_{\text{disk}} + (-9.335 \pm 13.569), \quad (1)$$

where the 90% confidence intervals of the slope and intercept are computed with the Jackknife resampling (Quenouille 1949, 1956; Tukey 1958). Notably, the slope of the relation is ~ 1 , which suggests that the value of θ_{BLR} of a source is expected statistically to be close to its θ_{disk} . Nevertheless, a null hypothesis test of the slope being 1 returns a p -value of 0.232 (i.e., 77% confidence), and we stress that, according to our Monte Carlo simulations that take the errors into consideration, the correlation, and hence the significance of the regression, is marginal.

Only eight sources are included in this work. The current analysis clearly suffers from insufficient data and the inhomogeneity of the type 1 AGN sample, which clusters toward inclinations below 50° . Indeed, we are fortunate that most sources have θ_{disk} around $30^\circ \pm 10^\circ$, which is close to the average value of θ_{BLR} , in order to return a somewhat strong positive correlation coefficient close to 1. To illustrate how tenuous the current results are, note that, for instance, if a point with $\theta_{\text{BLR}} \approx \theta_{\text{disk}} = 10^\circ$ were added to the current sample, the correlation coefficient would rise to 0.897 and the significance level to 3.28σ . Instead, if a point with $\theta_{\text{BLR}} \approx \theta_{\text{disk}} = 75^\circ$ were to be introduced, the

correlation coefficient and significance level would be boosted to 0.964 and 4.20σ , respectively. A major challenge of this work stems from the fact that we have restricted our analysis to sources that do not experience strong X-ray obscuration, to ensure that the spectral fits can successfully derive the inclinations; otherwise, seldom can we manage to interpret the spectra with a correct model for any measurement. Firmer conclusions on the relationship between BLR and accretion disk inclination must await future analysis with a significantly larger number of sources.

3.2. Caveats for the Accretion Disk Inclination

The uncertainties on θ_{disk} span a wide range related to their statistical and systematic aspects.

3.2.1. Statistical Uncertainties

In practice, the reliability of θ_{disk} measurements is heavily influenced by factors including the number of spectral epochs available for analysis and the simultaneity of observations from different instruments; the reflection fraction of the source also matters, as do the iron abundance and the coronal temperature (Du et al. 2024). However, R_f usually stands out as the major factor (Du et al. 2024). As a result of these complications, directly comparing the error bars on θ_{disk} among the eight sources is hardly instructive. Limiting to the statistical behaviors, we highlight this difficulty with two concrete examples.

With five epochs of nonsimultaneous observations (one from XMM-Newton, four from NuSTAR), MCG +04–22–042 has one of the smallest errors in our sample. In comparison, PG 1310–108, with only one epoch of XMM-Newton observation, has nearly the largest error. Without NuSTAR providing information about the higher energy band, it is hard to model the entire reflection continuum correctly in the absence of the Compton hump (e.g., Fabian et al. 2015; Du et al. 2024). Moreover, as per Du et al. (2024), R_f can be treated as a qualitative indicator for underlying uncertainties of the spectral fittings. From this perspective, we can anticipate that MCG +04–22–042, which has three epochs characterized by $R_f \gtrsim 1-3$, would yield a more robust estimate of θ_{disk} than PG 1310–108, which only has an upper limit of $R_f < 2.02$. Additionally, A_{Fe} and kT_e of MCG +04–22–042 are also higher than those of PG 1310–108, consistent with the more prominent reflection continuum in the former, even though the effect of these factors is not as significant as the reflection fraction.

However, if the comparison is drawn between PG 2209+184 and PG 1310–108, where the former has a slightly bigger error on θ_{disk} , the conclusion is less

straightforward. Two sources have roughly equal A_{Fe} . Yet, the coronal temperature of PG 2209+184 is higher than that of PG 1310–108. Despite having one epoch of simultaneous XMM-Newton and NuSTAR observations compared with the single XMM-Newton epoch of PG 1310–108, PG 2209+184 has a larger error on θ_{disk} . Here, R_f may play a more critical role than data combination in explaining this discrepancy, as PG 2209+184 has $R_f \approx 0.42$, while PG 1310–108 has $R_f \approx 0.88$ as the 50% value on the MCMC chain.

3.2.2. Systematic Uncertainties

As for systematic concerns, the main problem is the correct attribution of the intrinsic, reflected spectra and other contaminants, for instance, reprocessed emission like absorbers and thermal and nonthermal radiation directly from the accretion flow. We address the bias introduced by absorption in Section 3.3, and the bias introduced by soft excess modeling in Section 3.4. Here, we discuss the potential biases from the reflection model itself.

Theoretically, three factors introduce degeneracies to inclination measurements and the overall spectral fitting. The θ_{disk} in reflection models is degenerate with the spin and the radial emissivity profile due to their mutual effects on producing the broad Fe K α line and the Compton hump, and likely the soft excess. Atop these, the broadband spectra are tuned by the ionization state of the disk nonmonotonically (e.g., see Bonson & Gallo 2016; Reynolds 2021), which might lead to equally satisfactory fits with both a high and a low ionization state.

We have found that a_* has little effect on the recoverability of θ_{disk} by fitting generated mock spectra with known input parameters (Section 5.4 in Du et al. 2024), though the constraints on a_* itself and the complicated interplay between a_* and spectral features are still open topics (e.g., Reynolds 2021).

The radial emissivity profile is largely determined after selecting a flavor of coronal configuration within the RELXILL where the profile can be parameterized for various geometries (e.g., Dauser et al. 2013). For our choice of RELXILLCP, the empirical emissivity scales at $r^{-\text{Index}_1}$ between R_{in} and R_{br} and $r^{-\text{Index}_2}$ between R_{br} and R_{out} . The usually discovered high inner emissivity index ($\text{Index}_1 \gtrsim 5$ to 7; as also in our Table 2) has motivated the lamppost geometry (as in RELXILLP) which describes an isotropically irradiating source located on the rotational axis of the BH in its vicinity (e.g., Wilkins & Fabian 2011; Dauser et al. 2012; Miller et al. 2015; Beuchert et al. 2017). However, the configuration of the corona is still largely unclear and difficult to distinguish from spectral analysis especially when in-

tending to systematize the methodology on large samples (e.g., Bonson & Gallo 2016; Tortosa et al. 2018), even though several attempts in X-ray reverberation mapping (e.g., Reynolds et al. 1999; Fabian et al. 2009; Kara et al. 2016; Caballero-García et al. 2020) and spectropolarimetry as performed by the Imaging X-ray Polarimetry Explorer (IXPE, Weisskopf et al. 2022; e.g., Tagliacozzo et al. 2023; Gianolli et al. 2024a,b; Mondal et al. 2024; Serafinelli et al. 2024, however, see Ingram et al. 2023) have showcased their potential in resolving this intricacy with additional information beyond spectroscopy. For our purpose, adopting RELXILLCP with two emissivity indices and the broken radius implicitly takes into consideration of the coronal geometry without additional assumptions but increases the flexibility of the model than applying the lamppost geometry where several corona-related parameters are directly computed, and thus, careful source by source analysis (as in Appendix A) is needed for θ_{disk} measurements based on the reflection model.

For the degeneracy associated with ξ , we should also take on careful approaches to explore the parameter space of ξ source by source to reduce possible biases. This problem is also entangled with other absorbing or obscuring components, such as the WAs. But, according to Kammoun et al. (2018), if the absorbers are added correctly for high-quality broadband spectra exhibiting notable reflection features (e.g., $a_* > 0.8$, and lamppost corona height $h > 5 r_g$), the spectral fits should not be significantly affected.

3.2.3. Other Concerns

Regarding the validity of the reflection model itself, the simulation recipes are based on a thin constant density slab in local thermal equilibrium. However, real accretion disks exhibit more complex structures, including variations in the density profile, vertical stratification, magnetic fields, and radiation pressure, none of which are taken into account in current models. The impact of these factors on the reflection spectrum remains uncertain. Moreover, the accuracy of the reflection model is limited by the quality of the atomic data and radiative transfer calculations (e.g., García et al. 2013; Ding et al. 2024). For instance, parameters such as A_{Fe} , θ_{disk} , and disk density might be biased even if the model achieves a statistically acceptable fit. This limitation arises due to the omission of plasma physics effects that become significant in the soft energy regime at accretion disk densities of $\sim 10^{15} - 10^{22} \text{ cm}^{-3}$ (Ding et al. 2024).

Strictly speaking, the θ_{disk} measurements pertain to the innermost regions of the accretion disk, where the gravitational field of the black hole strongly influences

Table 4. Parameter Values of the Simulation Grid

Parameter	Input Range
$\log N_{\text{H}}$	{19, 20, 21, 22, 23}
$\log \xi_{\text{WA}}$	{-2, -1, 0, 1, 2, 3}
v/c	-0.05
θ_{disk}	{5, 25, 45, 65, 85} $^\circ$
a_*	{ ± 0.998 , ± 0.9 , ± 0.5 , 0}
R_f	{0, 0.3, 1, 5, 10}
A_{Fe}	$3 A_\odot$
Γ	2
$\log \xi$	3
kT_e	85 keV
Index ₁	7
Index ₂	3
R_{br}	$10 r_g$

the surrounding gas, leading to the broadening of emission lines. These broadened profiles encode the velocity field projection, and thus provide a measurement of the inclination of gas orbits. Therefore, our analysis, which correlates θ_{BLR} with θ_{disk} , implicitly examines the underlying relationship between the BLR and the inner accretion disk. It is worth noting that the accretion disks could be tilted or even fragmented into multiple sub-disks (see, e.g., simulations of tilted disks in Liska et al. 2021). Such structural complexities are not considered in the standard physical models of either the BLR or the X-ray reflection framework, nor are they directly addressed in this study.

3.3. Bias from the Warm Absorbers

Modeled with XSTAR tables, the WAs in our spectral fittings reprocess the intrinsic spectra, potentially mimicking the relativistic effects that influence θ_{disk} . To assess the impact of WAs on inclination measurements, we perform analyses on mock spectra simulating a single-epoch simultaneous observation of a nearby type 1 AGN. This approach evaluates the systematic biases introduced by the WAs in parameter retrievals. Alternatively, X-ray reverberation mapping could be employed to disentangle the reflection spectrum from absorption features (e.g., Fabian et al. 2009; Kara et al. 2016), but it is beyond the scope of this work.

Similar to the analysis in Section 4 of Du et al. (2024), we generate mock spectra with the baseline model CONSTANT*XSTAR*(ZBBODY+RELXILLCP) using the `fakeit` method in PYXSPEC (Arnaud 1996, 2016). The mock spectra are produced in the 0.3–10 keV

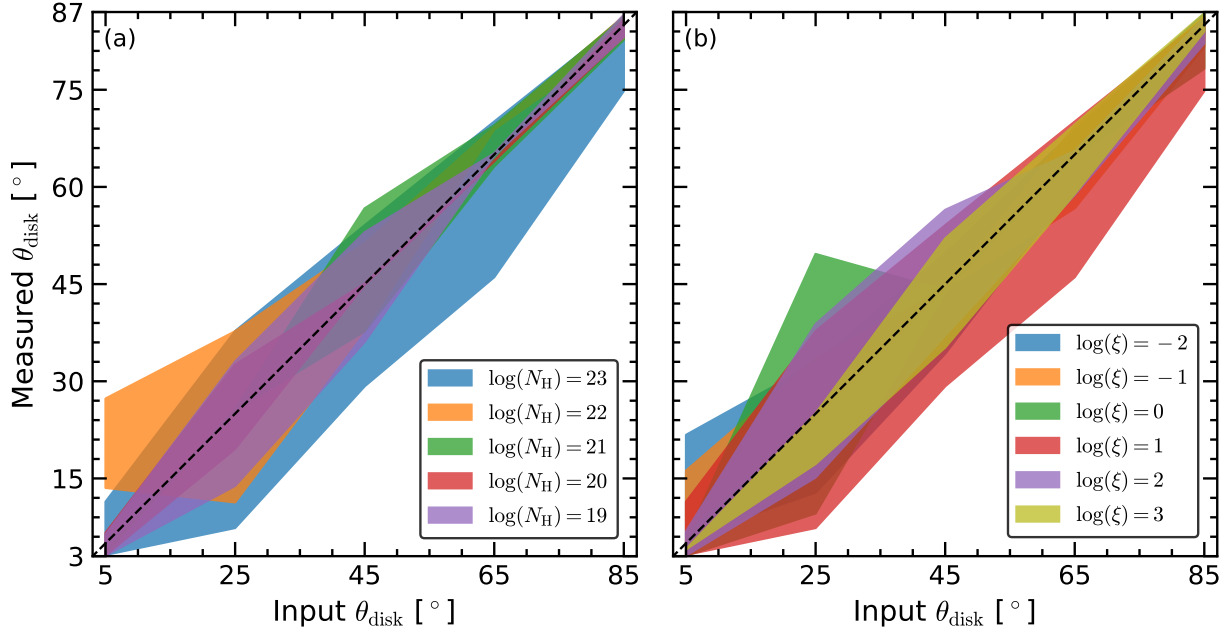


Figure 2. Inner accretion disk inclination measurements for simulated spectra with different WA values of (a) column density and fixed WA ionization at $\log \xi_{\text{WA}} = 1$, and (b) different values of WA ionization ξ_{WA} and fixed column density at $\log N_{\text{H}} = 23$. In all panels, we are showing the slice of parameter space with spin $a_* = 0.998$ and reflection fraction $R_f = 1$.

band of XMM-Newton/EPIC and the 3–78 keV band of NuSTAR, with background, response, and ancillary files from an observation epoch of 3C 382 (XMM-Newton: 0790600301, NuSTAR: 60202015006). The source exposure and background exposure times are set to 25 ks. The inner radius of the accretion disk is set to the radius of the innermost stable circular orbit; the outer radius is set to $R_{\text{out}} = 400 r_g$; and the density is set to $n = 10^{15} \text{ cm}^{-3}$. The blackbody temperature is set to 0.1 keV. The redshift is set to $z = 0.05557$ (van den Bosch et al. 2015). Other parameters are initialized as shown in Table 4, from which we create 5,250 distinct spectra.

The column density (N_{H}) and ionization parameter (ξ_{WA}) of the WA span the physical ranges typically observed in AGNs (e.g., Laha et al. 2021). The velocity is set to $v/c = -0.05$, consistent with commonly observed outflowing features (e.g., Braitto et al. 2014). The inclination angle is varied from nearly face-on to nearly edge-on configurations. BH spin ranges from +0.998 to -0.998, covering extreme prograde to non-rotating (Schwarzschild), and to extreme retrograde cases. Reflection fractions are set to 0, 0.3, 1, 5, and 10, representing non-reflection, “reflection-subordinate”, equal reflection and continuum, “reflection-dominant”, and highly reflected scenarios, respectively (Du et al. 2024). The iron abundance is set to three times the solar value, with a photon index of two and an ionization parameter of three, all consistent with observed AGN ranges.

The coronal temperature kT_e is fixed at 85 keV, adopted around the average of measurements in previous study (Kamraj et al. 2022). The emissivity profile is modeled as a broken power law with indices of $\text{Index}_1 = 7$ and $\text{Index}_2 = 3$, and the broken radius $R_{\text{br}} = 10 r_g$.

The mock spectra are fit using the same baseline model with technical setups applied for single-epoch, joint XMM-Newton and NuSTAR observations. Given the known input parameters, initiating the fit directly at the input values or randomizing the initial conditions for the MCMC error calculations is inappropriate (e.g., Bonson & Gallo 2016; Choudhury et al. 2017). Instead, we perform a preliminary fit and configure the proposal distribution for the MCMC chains in XSPEC as a Gaussian with a diagonal covariance matrix derived from 100 times the step length of the parameters in the preliminary fit. This approach ensures the sampler to explore the parameter space but without becoming trapped in local minima, especially for the flexible and complex baseline model in use. The MCMC chains are run with 200 walkers, generating at least 6×10^5 elements, with the first 10% discarded as burn-in to ensure convergence.

Building on the discussion in Du et al. (2024) regarding the influence of R_f , A_{Fe} , kT_e , and a_* on θ_{disk} measurements, our analysis focuses specifically on the effects of WAs. Results from two slices of the simulation grid are visualized in Figure 2 as representative examples. Overall, the inclination measurements are robust against the inclusion of WAs. The column density of

the WA exhibits a minor effect, with errors in θ_{disk} decreasing as N_{H} increases. This trend, which worsens measurements for denser WAs, reflects competition between intrinsic reflection and reprocessed emission in the spectral fitting. However, this effect becomes significant only at extreme column densities, $\log N_{\text{H}} = 22$ to 23, and primarily affects only θ_{disk} , with negligible impacts on a_* and R_f . The WA ionization parameter has an insignificant influence on the results. Across the entire simulation grid of 5,250 spectra, 94% exhibit an absolute inclination offset smaller than 5° between measured and input values; 98% have offsets smaller than 10° ; and 54% have 90% confidence intervals that encompass the input value with offsets smaller than 5° . All reduced fit statistics are below 1.05.

The most robust approach to studying parameter behavior is to generate mock spectra with identical spectral coverage to actual observations and with known input parameters over a fine grid encompassing the parameter space of interest, followed by blind fitting with the same model. However, this method is computationally intensive and time-consuming, necessitating practical compromises. Previous studies (Bonson & Gallo 2016; Choudhury et al. 2017; Kammoun et al. 2018; Du et al. 2024) have systematically tested parameter recovery with mock spectra. While the first three focused on a_* accuracy, Du et al. (2024) emphasized θ_{disk} reliability. Notably, only Kammoun et al. (2018) incorporated WA effects, using 60 mock spectra with more complex components, including warm and neutral absorbers, relativistic (RELXILLP) and distant (XILLVER) reflection, and thermal emission. Their simulations involved three collaborators: each of the one generating the spectra and two others independently fitting them, closely mimicking real observational procedures. They concluded that neither absorbers nor a_* significantly influenced the fits, though the lamppost height in RELXILLP did. Our work builds on these efforts, employing a larger simulation grid with a simplified fitting and error calculation approach compared to Kammoun et al. (2018). However, our primary aim is to evaluate the reliability of θ_{disk} measurements rather than exhaustively exploring the entire parameter space or probing the recovery and degeneracies of all baseline model parameters.

3.4. Bias from Treatments of the Soft Band

In our spectral fits, an epoch-independent blackbody is employed to model a portion of the soft excess. While effective, this is a simplified approach, as the exact na-

ture of the soft excess remains a topic of active debate (e.g., Crummy et al. 2006; Done et al. 2012; Jin et al. 2017; García et al. 2019; Gliozzi & Williams 2020; Petrucci et al. 2020). Current explanations for the soft excess include relativistically smeared reflection features at soft energies (e.g., García et al. 2019), Comptonization in a warm corona (e.g., Petrucci et al. 2020), or a combination of both. Additionally, complex absorption and scattering phenomena in the soft band can mimic relativistic effects typically associated with reflection, as discussed in Section 3.3.

In our analysis, the soft excess has been modeled with a simple, phenomenological redshifted blackbody. This approach has been demonstrated to work effectively in Section 5.7 of Du et al. (2024), provided that the WAs are accurately characterized using high-quality broadband spectra. In this section, we evaluate how different treatments of the soft excess influence inclination measurements.

Since Mrk 50 is well-represented by pure reflection without requiring a blackbody or WA component, we exclude it from this test. For all other sources, we refit the spectra using the Comptonization component NTHCOMP (Zdziarski et al. 1996; Życki et al. 1999) in XSPEC to model the soft excess in place of ZBBODY. The asymptotic power-law photon index Γ_c , electron temperature kT_{ce} , and seed photon temperature kT_{cbb} are set as free parameters, with the seed photons assumed to originate from a disk blackbody. The reflection model remains unchanged, meaning that the substitution introduces two additional parameters into the model. Errors are computed using the MCMC approach described in Section 2.4.

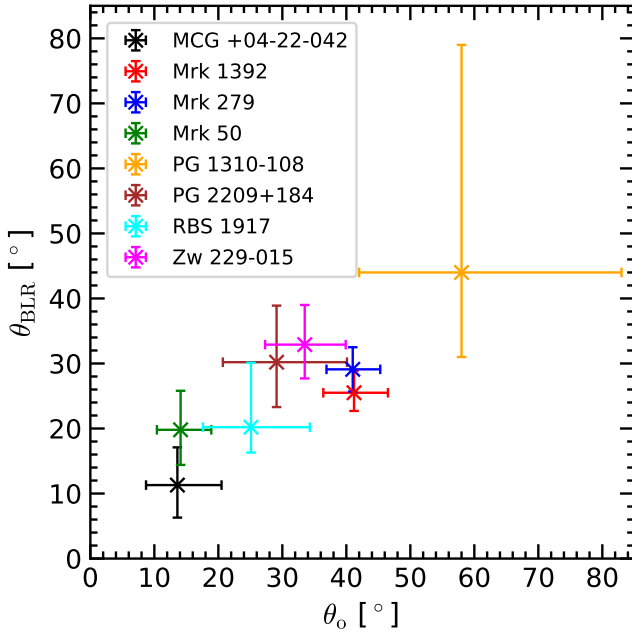
Table 5 summarizes the results, including the blackbody temperature (kT), θ_{disk} , and χ^2 values for the fits. Substituting the blackbody with the Comptonization component does not lead to significant deviations in the inclination measurements. Similarly, R_f and ξ remain consistent with the baseline model. Despite the addition of two free parameters, the fit statistics are not substantially improved—and in some cases, slightly worsen—indicating potential overfitting or insufficient physical motivation for the Comptonization component.

In conclusion, based on current data quality, the treatment of epoch-independent blackbody provides a sufficiently accurate representation of the soft excess, with negligible influence on inclination measurements compared to the Comptonization component at the current level of spectral quality and fit precision. Nevertheless, we emphasize the importance of accurate soft-band modeling in enhancing the precision of reflection model fits. Arbitrary treatments of the soft band should be

Table 5. Parameters Used to Interpret the Soft Excess

Name	kT	θ_{disk}	χ^2	DOF	Γ_c	kT_{ce}	kT_{cbb}	θ_{disk}	χ^2	DOF
	(keV)	($^\circ$)				(keV)	(eV)	($^\circ$)		
(1)	(2)	(3)	(4)	(5)	(6)	(7)	(8)	(9)	(10)	(11)
MCG +04–22–042	$0.165^{+0.034}_{-0.022}$	$15.2^{+2.2}_{-1.5}$	1651.6	1655	$9.37^{+0.31}_{-0.34}$	$1.62^{+0.08}_{-0.09}$	224^{+10}_{-11}	$16.5^{+0.2}_{-0.3}$	1650.4	1653
Mrk 279	0.089 ± 0.004	$26.9^{+2.5}_{-3.7}$	1327.9	1186	$8.50^{+0.09}_{-0.10}$	$1.62^{+0.09}_{-0.08}$	106^{+4}_{-2}	$25.8^{+0.9}_{-1.0}$	1337.3	1184
Mrk 1392	$0.040^{+0.005}_{-0.008}$	$25.5^{+6.7}_{-9.9}$	453.1	401	8.65 ± 0.13	$42.5^{+0.5}_{-0.4}$	$22.4^{+0.1}_{-0.2}$	$26.2^{+0.1}_{-0.5}$	454.1	399
PG 1310–108	$0.089^{+0.007}_{-0.010}$	$33.5^{+20.8}_{-22.4}$	389.6	373	4.13 ± 0.21	$2.13^{+8.08}_{-1.10}$	$1.4^{+8.8}_{-0.4}$	$38.7^{+0.8}_{-2.1}$	435.1	371
PG 2209+184	$0.086^{+0.015}_{-0.017}$	$35.6^{+31.7}_{-25.9}$	1023.0	915	$4.63^{+0.86}_{-0.64}$	$9.62^{+28.9}_{-8.29}$	$7.8^{+46.0}_{-6.7}$	$40.3^{+6.1}_{-8.9}$	1031.5	913
RBS 1917	$0.248^{+0.009}_{-0.031}$	$17.2^{+4.5}_{-1.1}$	410.7	351	2.50 ± 0.01	> 300	139 ± 1	17.0 ± 0.01	490.1	349
Zw 229–015	0.103 ± 0.001	$26.2^{+2.5}_{-0.5}$	471.2	463	$3.77^{+0.04}_{-0.02}$	1.62 ± 0.01	5.4 ± 0.1	$29.0^{+0.8}_{-0.5}$	479.4	461

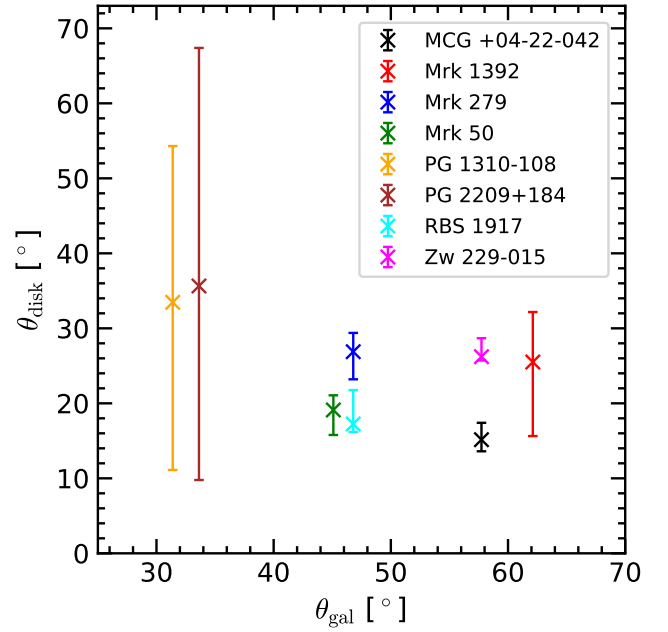
NOTE— Col. (1): Name of the source. Col. (2): Temperature of the epoch-independent blackbody (see Appendix A). Col. (3): Inclination of the inner accretion disk when the blackbody is used (Column 3 of Table 2). Col. (4): χ^2 statistic of the fit with the blackbody. Col. (5): Degrees of freedom of the fit with the blackbody. Col. (6): Power-law photon index of the Comptonization component (NTHCOMP). Col. (7): Electron temperature of the Comptonization component. Col. (8): Seed photon temperature of the Comptonization component. Col. (9): Inclination of the inner accretion disk when the Comptonization component is used. Col. (10): χ^2 statistic of the fit with the Comptonization component. Col. (11): Degrees of freedom of the fit with the Comptonization component.

**Figure 3.** The relation between the BLR inclination versus its opening angle.

avoided, as they could inadvertently affect the reliability of θ_{disk} measurements.

3.5. Error on the BLR Inclination

Similar to the accretion disk measurements, the errors of the BLR inclination angles also vary among the sources. Under most circumstances, the CAMEL

**Figure 4.** The relation between the inclination of the inner accretion disk versus the large-scale inclination of the galactic disk. Errors for the galactic disk inclination are not shown.

models give formal errors of $5^\circ - 10^\circ$ for θ_{BLR} (Table 3). However, the full dynamical model of the BLR is complex and has many parameters and underlying assumptions whose uncertainties are difficult to quantify. For instance, the CAMEL framework ignores the effect

of radiation pressure on the dynamics of the gas. As the radiation pressure has a radial dependence similar to gravity, omitting it can underestimate the BH mass (Marconi et al. 2008; Pancoast et al. 2014a; Villafaña et al. 2022). The model adopts simplified dynamics for point particles, neglecting detailed structures of the BLR and other lower order factors such as self-gravity, gas viscosity, and interactions between the BLR and accretion disk gas. The actual BLR might have multiple sub-structures with different geometries and dynamics (e.g., Baldwin et al. 1995; Collin et al. 2006), each with slightly different inclination and kinematics. By necessity, the inclination results we use are only phenomenological averages of the BLR traced by the $H\beta$ line. This oversimplification obviously can introduce subtle errors in θ_{BLR} .

Another complication is that the other geometric parameter in the model—the opening angle θ_o —can be related closely to and hence affecting the precision of θ_{BLR} . Figure 3 plots θ_{BLR} against θ_o , where we have taken the opening angle measurements (Table 3) directly from Williams et al. (2018) and Villafaña et al. (2022). The Pearson correlation coefficient is 0.882 with a p -value of 0.004, indicating a strong positive correlation between θ_o and θ_{BLR} at the level of 2.9σ . It is thus likely that θ_o and θ_{BLR} are not independent in the geometrical description of the system. Naturally, θ_{BLR} is more difficult to constrain precisely when θ_o is large. It is hard to distinguish between a geometrically thick BLR that is face-on or edge-on. Furthermore, since the two parameters affect the projection of the velocity field onto the line-of-sight in opposite ways, dynamical modeling of a thick, extended BLR may require a corresponding inclination for compensation in order to match the observed velocity profiles. This correlation was first identified by Grier et al. (2017), who noted that the model required a positive relationship between the inclination angle and the opening angle to reproduce the observed emission-line profiles. This dependency arises from the distribution of the transfer function in wavelength and time-lag space. A potential method to disentangle this degeneracy involves interferometric observations, as demonstrated by GRAVITY Collaboration et al. (2020), which could provide more direct constraints on the BLR geometry and kinematics.

There is no significant correlation between the error of θ_{BLR} and the value of θ_o (correlation coefficient 0.600, p -value 0.116). The moderate correlation suggests that θ_o might affect the precision of θ_{BLR} secondarily or non-linearly, as other parameters such as the BLR radial profile and velocity field could also have simultaneous impact, as do purely geometric factors. The correlation

coefficient of the error of θ_{BLR} and the error of θ_o is 0.977 with a p -value of 3×10^{-5} , which is significant at 4.2σ . The mutual growth in the size of the error bars is evident in the plot. The very strong correlation between the errors implies that the uncertainties in θ_o may have propagated directly into the uncertainties in the inclination angle, and vice versa, suggesting that the BLR geometry is more likely determined by the mutual effects of the inclination and the opening angle on the velocity field projection.

3.6. Connection to Galactic Scales

If the inclination correlation on the scale of the BLR and accretion disk can be confirmed, then inclination measurements on small scales can be used to test for (mis)alignment with the galactic disk on large scales, as a means of probing the fueling mechanism and cosmological evolution of active galaxies (e.g., Hopkins et al. 2012). As a demonstration based on this work, we compare the inner accretion disk inclination and BLR inclination with the galactic disk inclination θ_{gal} to examine whether the angular momentum of different scales in active galaxies are related. Here, we assume that the galactic disk inclination serves as a proxy for the large-scale angular momentum of the host galaxy (\mathbf{J}_{gal}), and that the inclination of the inner accretion disk tracks the small-scale angular momentum of the central BH (\mathbf{J}_{BH}). The alignment ($\mathbf{J}_{\text{gal}} \parallel \mathbf{J}_{\text{BH}}$ or $\mathbf{J}_{\text{gal}} \cdot \mathbf{J}_{\text{BH}} \approx |\mathbf{J}_{\text{gal}}||\mathbf{J}_{\text{BH}}|$) or misalignment ($\mathbf{J}_{\text{gal}} \cdot \mathbf{J}_{\text{BH}} < |\mathbf{J}_{\text{gal}}||\mathbf{J}_{\text{BH}}|$) of the two angular momenta are then simplified to the alignment or misalignment of the two inclinations, which may offer insights into the feeding mechanism of the supermassive BH. Alignment requires systematic, long-term co-planar fueling (e.g., King et al. 2005), whereas misalignment might result from mergers that knock the BH spin off the host galaxy plane (e.g., Gerosa et al. 2015), if the Bardeen & Petterson (1975) effect has not yet aligned the accretion flow with the BH spin.

We calculate galaxy inclination angles (Table 3) using K_s band images from the Two Micron All Sky Survey (2MASS, Skrutskie et al. 2006). The galactic inclination follows from (Hubble 1926)

$$\cos \theta_{\text{gal}} = \sqrt{\frac{q^2 - q_0^2}{1 - q_0^2}}, \quad (2)$$

with $q = b/a$ the minor-to-major axis ratio (Jarrett et al. 2000) measured with isophotal photometry set at $20 \text{ mag arcsec}^{-2}$ in the K_s band, and q_0 the intrinsic axis ratio assumed to be 0.2 (Holmberg 1946; Guthrie 1992, see Yu et al. 2020 for a more complex treatment). Plotting θ_{disk} against θ_{gal} reveals no obvious trend (Figure 4). The Pearson correlation coefficient between θ_{disk}

and θ_{gal} is -0.597 with a p -value of 0.118 , and the correlation coefficient between θ_{BLR} and θ_{gal} is -0.540 with a p -value of 0.167 . The lack of statistical significance suggests that no meaningful relationship holds between the inclinations on very large and small scales in active galaxies, at least within our limited sample. Kormendy & Ho (2013, their Section 3.3.3) and Wu et al. (2022) reached a similar conclusion. These indicate the possible existence of a diverse AGN feeding mechanisms of both coplanar accretion and minor mergers.

A closely related investigation that arrived at somewhat different results was conducted by Middleton et al. (2016), who found a loose (3σ) correlation between the inner accretion disk inclination based on previous reflection modeling and the galactic stellar disk inclinations mainly taken from HYPERLEDA (Makarov et al. 2014) for their sub-sample of 21 AGNs. Yet, their complete sample of 26 AGNs returned lack of correlation at $\gg 5\sigma$. In a recent extensive study of the position angle differences between radio and optical images of radio AGNs, Zheng et al. (2024) conclude that jet alignment depends on radio power and galaxy shape: the jets of low radio power tend to show preferential alignment with the minor axis of optically more flattened host galaxies.

4. SUMMARY

We investigate the relationship between the inclination angle of the inner accretion disk and the BLR in AGNs. Starting with type 1 AGNs with published BLR inclination measurements derived from velocity-resolved RM campaigns, we closely follow the methodology of Du et al. (2024) to analyze the broadband $0.3\text{--}78\text{ keV}$ spectra of a small sample of eight sources with sufficient data for X-ray reflection spectroscopic analysis using the self-consistent reflection model RELXILLCP. The RM results provide measurements of θ_{BLR} , while our spectral fits derive θ_{disk} . While the two inclinations show a strong, positive correlation (Pearson correlation coefficient 0.856 , p -value 0.007), the correlation is marginal ($< 3\sigma$) according to our Monte Carlo simulations. Nevertheless, a nearly linear relation between θ_{BLR} and θ_{disk} revealed by our regression analysis hints at a possible alignment between the accretion disk and the BLR, which has a number of implications, including the possibility of elucidating physical models that link these two fundamental components of the central engine of active galaxies. An alignment between these two fundamental components of AGNs would suggest that the rotational axes of the BLR and the accretion disk are likely the same. Moreover, on account of the Bardeen-

Petterson effect, this common rotation axis should also be the orientation with respect to the line-of-sight for the BH spin. If more sources with θ_{disk} spanning $0 - \pi/2$ can be added in the future to support the correlation, we would be able to claim that the BLR, believed to emanate from near or above the accretion disk, is closely related to the accretion disk or potentially shaped by the same axisymmetric environment as the accretion disk.

While disk wind models are often invoked to explain the formation of the BLR (e.g., Peterson 2006), debate continues as to whether the disk winds derive from radiation pressure-driven outflows or magnetically driven outflows (e.g., see Czerny & Hryniewicz 2011). In any case, the disk winds should connect the BLR with the accretion disk in many physical aspects. We note, in passing, that all seven of the sources in our sample that show evidence for WAs (Table A1) have outflows, whose velocities exceed $0.1c$ in four cases (MCG +04–22–042, Mrk 1392, PG 1310–108, and Zw 229–015). This could be expected if BLR clouds indeed form from launched disk winds, similar to those that produce the WAs. Previous BLR dynamical modeling of RM observations (Pancoast et al. 2014b) find that the broad emission lines on the far side of the accretion disk are hidden by optically thick material, which can plausibly be associated with disk winds (e.g., Shields 1977; Murray & Chiang 1995; Elvis 2017) because WAs are observed as blueshifted absorption lines in both the X-ray and UV.

ACKNOWLEDGEMENTS

We thank the anonymous referee for helpful suggestions. This work was supported by the National Key R&D Program of China (2022YFF0503401), the National Science Foundation of China (11991052, 12233001), and the China Manned Space Project (CMS-CSST-2021-A04, CMS-CSST-2021-A06). This research has made use of the NASA/IPAC Extragalactic Database (NED), which is funded by the National Aeronautics and Space Administration and operated by the California Institute of Technology. We thank Jinyi Shangguan for helpful comments.

Facilities: XMM-Newton, NuSTAR

Software: ASTROPY (Astropy Collaboration et al. 2013, 2018, 2022), EMCEE (Foreman-Mackey et al. 2013), MATPLOTLIB (Hunter 2007), NUMPY (van der Walt et al. 2011; Harris et al. 2020), SCIENCEPLOTS (Garrett 2021), XSPEC & PYXSPEC (Arnaud 1996, 2016)

APPENDIX

Table A1. Best-fit Parameters for the Warm Absorbers

Source	N_{H} (10^{20} cm^{-2})	$\log \xi_{\text{WA}}$ (erg cm s^{-1})	v/c
(1)	(2)	(3)	(4)
MCG +04–22–042	$12.92^{+3.30}_{-3.32}$	$1.42^{+0.23}_{-0.20}$	$0.114^{+0.011}_{-0.015}$
Mrk 279	$30.46^{+6.65}_{-4.51}$	$2.44^{+0.11}_{-0.10}$	0.057 ± 0.009
Mrk 1392	$7.83^{+2.87}_{-1.90}$	$-1.52^{+0.26}_{-0.17}$	$0.129^{+0.040}_{-0.045}$
PG 1310–108	$3.12^{+6.74}_{-1.71}$	$0.33^{+1.12}_{-0.77}$	$0.181^{+0.029}_{-0.025}$
PG 2209+184	$3.87^{+4.66}_{-2.67}$	$1.56^{+0.66}_{-0.48}$	$0.041^{+0.032}_{-0.034}$
RBS 1917	$3.96^{+7.03}_{-3.28}$	$0.70^{+0.43}_{-0.41}$	$0.081^{+0.004}_{-0.016}$
Zw 229–015	$2.92^{+0.07}_{-0.24}$	$0.22^{+0.01}_{-0.05}$	$0.163^{+0.001}_{-0.006}$

NOTE— Col. (1): Name of the source. Col. (2): Hydrogen column density. Col. (3): Ionization parameter. Col. (4): Outflow velocity divided by the speed of light. The best-fit values and 90% confidence intervals are presented.

A. DETAILS ON X-RAY SPECTROSCOPY

In this appendix, we provide the details of our spectral fitting of the eight sources described in Sections 2.1 and 2.3, where the general procedure follows Section 2.4. We summarize the best-fit values of the continuum in Table 2 and the results of WAs in Table A1.

A.1. MCG +04–22–042

MCG +04–22–042 was observed by XMM-Newton once in 2006 for 122 ks (0312191401) but less than 10% of the observation time was effective. It was also observed by NuSTAR in 2012 (60061092002), 2020 (60602018002), March 2021 (60602018004), and June 2021 (60602018006). We use all five observation epochs (a–e). The NuSTAR data, even though not collected simultaneously with the XMM-Newton observation, provides information on the Compton hump and improves the fit of the entire reflection continuum. During the fit, we tie the disk-related parameters (θ_{disk} , a_* , and A_{Fe}) and fit the data jointly while setting free the corona-related parameters for each epoch.

We illustrate the broadband fitting procedure in Figure 5. In terms of reduced statistic (fit statistic over degrees of freedom, DOF), the blackbody plus reflection continuum improves the fit by $\Delta\chi^2/\Delta\text{DOF} = -386.8/-35$ compared to the phenomenological power-law ZPOWERLW. Further adding the WA returns $\chi^2/\text{DOF} = 1651.6/1655 = 0.998$ ($\Delta\chi^2/\Delta\text{DOF} = -16.1/-3$), which gives the best fit for this source. Although the likely diverse nature of the soft excess cannot

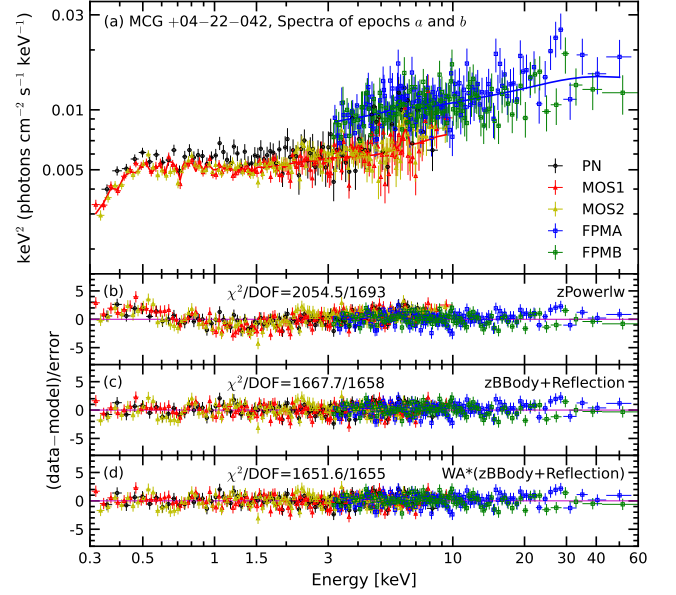


Figure 5. The XMM-Newton and NuSTAR broadband spectral fit of MCG +04–22–042, showing the best fit with the baseline model (a). All epochs are fit simultaneously. The residuals in terms of error sigmas are plotted for (b) the phenomenological redshifted power-law model, (c) RELXILLCP plus a redshifted blackbody component, and (d) RELXILLCP plus a redshifted blackbody component and a WA. For clarity, only the spectra of epoch a (PN, MOS1, MOS2) and epoch b (FPMA, FPMB) are shown.

be explained uniquely by the reflection model (Du et al. 2024), we suggest that an epoch-independent blackbody (ZBBODY), together with RELXILLCP, offers an acceptable description of the soft excess in most situations. In the case of MCG +04–22–042, the X-ray spectrum can be fit by a ZBBODY model with the blackbody temperature of $0.165^{+0.034}_{-0.022}$ keV. Subtracting this component from the best-fit model returns an inferior statistic of $\Delta\chi^2/\Delta\text{DOF} = +10.1/+2$. Our reflection model results in $\theta_{\text{disk}} = 15.2^{+2.2}_{-1.5}$ and $a_* = 0.996^{+0.002}_{-0.013}$. Because the reflection fractions of all five epochs are not very small ($0.3 \lesssim R_f \lesssim 3$; see Section 5.1. of Du et al. 2024, where $R_f < 0.3$ is considered reflection-subordinate) and all five epochs are fit jointly, the model values are calculated with rather high precision.

Three studies on X-ray properties of MCG +04–22–042 used XMM-Newton or NuSTAR. Winter et al. (2008) analyzed our first spectral epoch (a) and suggested that this XMM-Newton observation, together with another non-simultaneous epoch from the Swift X-Ray Telescope (XRT; Gehrels et al. 2004; Burrows et al. 2005), were well interpreted using an absorbed power-law model with pegged normalization (PEGPWRLW) at the photon index of $\Gamma \approx 2.00$. However, with their reduced statistic of

$\chi^2/\text{DOF} = 1534.8/1190 = 1.290$, their fit is not strongly favored statistically. Akylas & Georgantopoulos (2021) analyzed the NuSTAR spectra that belongs to our epoch *b* using a reflection model PEXMON (Nandra et al. 2007), which describes the neutral reflection of an exponentially cutoff power-law spectrum while self-consistently generating narrow Fe K lines. Fixing the disk inclination to 60° , they obtained a reduced statistic of 0.93 with $\Gamma = 1.92 \pm 0.06$ and a reflection scaling factor (equivalent to R_f) of $R = 0.53^{+0.24}_{-0.22}$. Kang & Wang (2022) interpreted the same NuSTAR data set with PEXRAV (Magdziarz & Zdziarski 1995), which also accounts for a neutral reflector. Assuming solar abundances and $\cos\theta_{\text{disk}} = 0.45$, they derived $\Gamma = 1.95^{+0.10}_{-0.09}$ and $R = 0.59^{+0.44}_{-0.33}$ with $\chi^2/\text{DOF} = 0.87$. Additionally, they used RELXILLCP to calculate the coronal temperature of $kT_e > 37 \text{ keV}$ at $\chi^2/\text{DOF} = 0.88$ while adopting maximal Kerr spin, neutral ionization state, and a disk inclination of 30° . Since their fits returned small reduced statistics, they may have underestimated the uncertainties of the parameters. Besides, notice that they arrived at a smaller lower limit of the coronal temperature than ours when using the same model but assuming the small $\xi = 0$ and the θ_{disk} around twice as large as ours. As another recent reflection spectroscopic analysis yet using data aside from the two observatories, Waddell & Gallo (2020) studied data from the Suzaku satellite (Mitsuda et al. 2007) and modeled the continuum with a power-law, a Compton hump, an Fe K α line, and a soft excess represented by a blackbody. They obtained a photon index of 1.88 ± 0.02 and a blackbody temperature ($kT = 0.13 \pm 0.01 \text{ keV}$) similar to ours, though with a slightly disfavored reduced Cash (1979) statistic of $C\text{-stat}/\text{DOF} = 290/248 = 1.17$. Despite different treatments of the reflection continuum, the results from these works are generally consistent with our findings. However, our analysis is conducted with as many as five epochs while setting as many parameters free as possible, including a_* and θ_{disk} which result in $0.996^{+0.002}_{-0.013}$ and $15^\circ.2^{+2.2}_{-1.5}$, respectively.

A.2. Mrk 50

Mrk 50 was observed by XMM-Newton once in 2009 and twice on 9 December 2010. We selected the most recent observation with the longest exposure time (0650590401, PI: L. Bassani; epoch *a*, 22.9 ks), and combined it with the 2022 NuSTAR observation (60061227002; epoch *b*).

The reflection plus blackbody model improves the phenomenological fit by $\Delta\chi^2/\Delta\text{DOF} = -455.6/-17$ (Figure 6). Yet, the blackbody component ($kT = 0.229^{+0.044}_{-0.069} \text{ keV}$), if removed, merely affects the fit

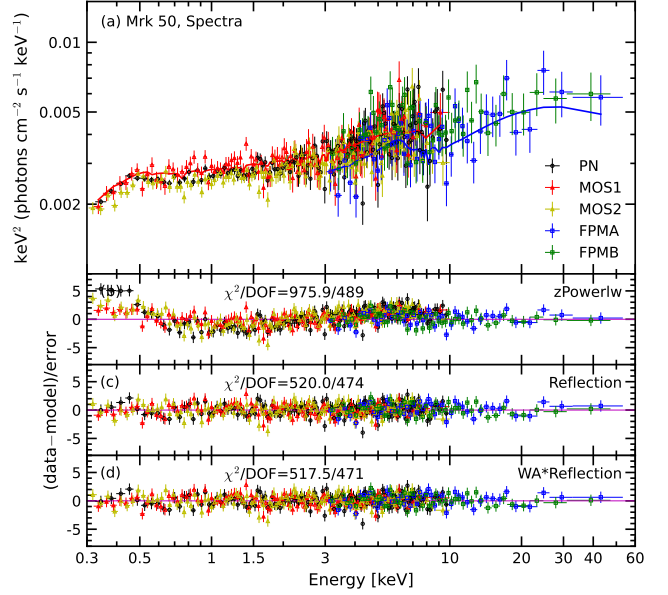


Figure 6. The XMM-Newton and NuSTAR broadband spectral fit of Mrk 50, showing the best fit with the baseline model (a). All epochs are fit simultaneously. The residuals in terms of error sigmas are plotted for (b) the phenomenological redshifted power-law model, (c) RELXILLCP, and (d) RELXILLCP plus a WA.

marginally by $\Delta\chi^2/\Delta\text{DOF} = +2.5/+2$, prompting us to reject this component. Further adding a WA component (Figure 6d; $\Delta\chi^2/\Delta\text{DOF} = -2.5/-3$) is also not well justified. This case requires a highly ionized ($\xi_{\text{WA}} \gtrsim 10^3 \text{ erg cm s}^{-1}$) WA with a column density of $N_{\text{H}} \gtrsim 7.55 \times 10^{22} \text{ cm}^{-2}$, which seems somewhat spurious because absorption in such an environment should be weak to barely detectable. Moreover, these parameter values are close to the limits of the XSTAR grid points, which can produce unreliable results. Given that the goodness-of-fit is not improved by the WA, we adopt the pure reflection model (Figure 6c; CONSTANT*TBABS*RELXILLCP) as the best fit, which has a statistic of $\chi^2/\text{DOF} = 520.0/474 = 1.10$. MCMC calculations give $\theta_{\text{disk}} = 19^\circ.1^{+2.0}_{-3.3}$ and $a_* = 0.992^{+0.005}_{-0.030}$.

Vasudevan et al. (2013) examined the 2009 XMM-Newton observation with both a phenomenological blackbody plus power-law ($\Gamma = 1.95 \pm 0.02$) model and the reflection model PEXRAV. With $\chi^2/\text{DOF} = 902.32/879 = 1.03$, they reported a soft excess but did not detect any absorption or iron emission. Fitting the XMM-Newton spectra jointly with an observation from the Swift Burst Alert Telescope (BAT; Barthelmy et al. 2005) with PEXRAV yielded $\Gamma = 2.18 \pm 0.02$ and $R = 4.79^{+0.96}_{-0.91}$, which is slightly larger than ours, although the authors froze the abundances to solar and

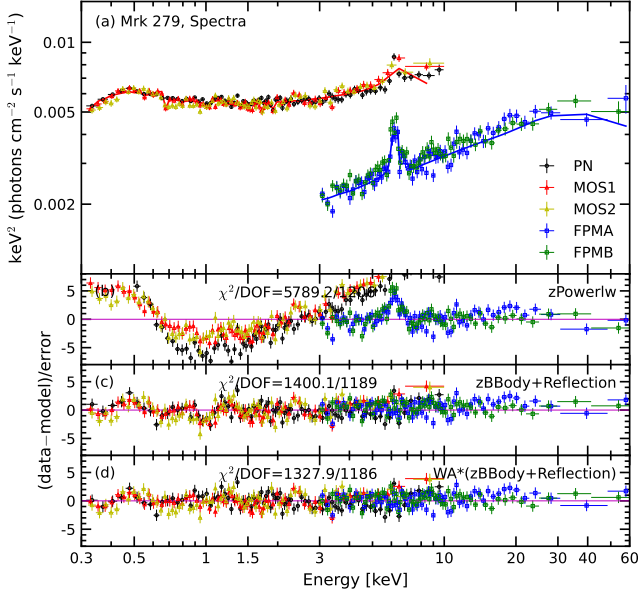


Figure 7. The XMM-Newton and NuSTAR broadband spectral fit of Mrk 279, showing the best fit with the baseline model (a). All epochs are fit simultaneously. The residuals in terms of error sigmas are plotted for (b) the phenomenological redshifted power-law model, (c) RELXILLCP plus a redshifted blackbody component, and (d) RELXILLCP plus a redshifted blackbody component and a WA. For plotting purposes, the XMM-Newton data have been rebinned to $S/N > 25$, while the NuSTAR data have been rebinned to $S/N > 15$.

the inclination angle to $\cos \theta_{\text{disk}} = 0.45$. Boissay et al. (2016) analyzed one of the 2010 XMM-Newton observations (epoch *a*) with two Bremsstrahlung components and a cutoff power-law with $\Gamma = 1.92^{+0.07}_{-0.13}$. They also calculated the reflection fraction to be $R_f = 1.75^{+0.55}_{-0.67}$ using RELXILLCP, which adopts a lamppost geometry (Matt et al. 1991; Martocchia & Matt 1996; Reynolds & Begelman 1997; Miniutti & Fabian 2004) instead of our sandwich (thin coronal layers) geometry (see Section 5.6 of Du et al. 2024 for more information on geometry selection).

A.3. Mrk 279

The newest XMM-Newton observation of Mrk 279 was conducted in December 2020 (0872391301; epoch *a*, 30.5 ks), and a long observation was completed by NuSTAR in August 2020 (60601011004; epoch *b*). The two epochs are characterized by significantly different (factor of ~ 2) luminosities. The reflection plus blackbody model improves the fit by $\Delta\chi^2/\Delta\text{DOF} = -4389.1/-17$ compared to the power-law model (Figure 7). Adding a WA returns a best-fit model statistic of $\chi^2/\text{DOF} = 1327.9/1186 = 1.12$ ($\Delta\chi^2/\Delta\text{DOF} = -72.2/-3$), while removing the blackbody component

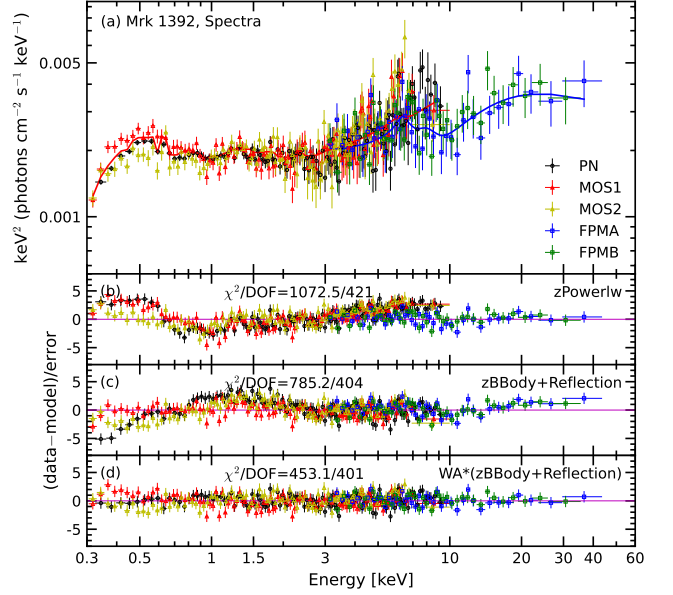


Figure 8. The XMM-Newton and NuSTAR broadband spectral fit of Mrk 1392, showing the best fit with the baseline model (a). All epochs are fit simultaneously. The residuals in terms of error sigmas are plotted for (b) the phenomenological redshifted power-law model, (c) RELXILLCP plus a redshifted blackbody component, and (d) RELXILLCP plus a redshifted blackbody component and a WA.

($kT = 0.089 \pm 0.004$ keV) from the best-fit model deteriorates the statistic by $\Delta\chi^2/\Delta\text{DOF} = +123.5/+2$. Our adopted reflection modeling results in $\theta_{\text{disk}} = 26^\circ.9^{+2.5}_{-3.7}$ and $a_* = 0.997^{+0.001}_{-0.006}$.

Historically, Mrk 279 has been known to be significantly variable in the X-rays from extensive observations by various missions (e.g., Scott et al. 2004; Costantini et al. 2010; Ebrero et al. 2010; Yaqoob & Padmanabhan 2004; Jiang et al. 2019; Igo et al. 2020; Ursini et al. 2020). Akhila et al. (2024) reported long-term X-ray analysis of this source during 2018–2020, including both epochs *a* and *b*. They fit epoch *a* with a blackbody component, a thermal Comptonization component (THCOMP; Zdziarski et al. 2020), a Gaussian line at 6.41 ± 0.04 keV, and a Compton scattering power-law (SIMPL; Steiner et al. 2009) with $\Gamma = 1.48^{+0.16}_{-0.21}$. Another fit for epoch *b* without the blackbody yielded $\Gamma = 1.62 \pm 0.01$. Ballantyne et al. (2024) studied three XMM-Newton observations from 2005 with the reflection model REXCOR (Xiang et al. 2022) with lamppost geometry at a fixed inclination of 30° , and obtained $a_* = 0.99$ and the lamppost coronal height varying from $20 r_g$ to $5 r_g$.

A.4. Mrk 1392

Mrk 1392 was observed by XMM-Newton on 20 January 2018 (0795670101, PI: G. Lansbury; epoch *a*, 38 ks)

and by NuSTAR on 25 January 2018 (60160605002; epoch *b*). As with MCG +04–22–042, even the non-simultaneous NuSTAR data can be useful for broadband modeling of the hard X-rays. Relative to the power-law model, the RELXILLCP plus blackbody model improves the phenomenological fit by $\Delta\chi^2/\Delta\text{DOF} = -287.3/-17$ (Figure 8). Adding a WA returns the best-fit model statistic of $\chi^2/\text{DOF} = 453.1/401 = 1.13$ ($\Delta\chi^2/\Delta\text{DOF} = -332.1/-3$). If removing the blackbody component ($kT = 0.040^{+0.005}_{-0.008}$ keV) from the best-fit model, the statistic deteriorates by $\Delta\chi^2/\Delta\text{DOF} = +9.6/+2$. Our preferred reflection model results in $\theta_{\text{disk}} = 25^\circ.5^{+6.7}_{-9.9}$ and $a_* = 0.942^{+0.038}_{-0.093}$.

Esparza-Arredondo et al. (2020) fit the NuSTAR spectra of epoch *b* using a single power-law with a partial covering absorber to account for Galactic absorption. Achieving $\chi^2/\text{DOF} = 1.12$, they reported $\Gamma = 1.84^{+0.05}_{-0.04}$, consistent with our results. Esparza-Arredondo et al. (2021) repeated the analysis using alternative models that account for reflection features caused by a distant reflecting torus. Their values of Γ are roughly compatible with previous results, but their smooth torus model (borus02; Baloković et al. 2018) returned an inclination of 87.0° , while their clumpy model (UXClumpy; Buchner et al. 2019) gave a markedly different inclination of 1.0° . Another difference between our analysis and theirs regards the interpretation of Galactic absorption. In their first paper, the measurement for the column density was $\log(N_{\text{H}}/\text{cm}^{-2}) = 24.63^{+0.16}_{-0.18}$; their subsequent work obtained a similar large value of N_{H} . We find substantially different results. Instead of fitting the Galactic absorption with a partial covering absorber, we use the TBABS model with a column density fixed to $\log(N_{\text{H}}/\text{cm}^{-2}) = 20.58$ from the Leiden/Argentine/Bonn Survey. We also find a WA with $\log(N_{\text{H}}/\text{cm}^{-2}) \approx 21$.

A.5. PG 1310–108

PG 1310–108 was observed by XMM-Newton once in 2018 for 21 ks (0801891601, PI: S. Kaspi). Lacking observations at higher energy, the sole EPIC spectrum is adopted as epoch *a* in our analysis. All disk and corona-related parameters are free to vary. The reflection plus blackbody model improves the power-law fit by $\Delta\chi^2/\Delta\text{DOF} = -1,208.8/-11$ (Figure 9). Including a WA yields a best-fit model statistic of $\chi^2/\text{DOF} = 389.6/373 = 1.04$ ($\Delta\chi^2/\Delta\text{DOF} = -17.3/-3$), while excluding the blackbody component with $kT = 0.089^{+0.007}_{-0.010}$ keV gives $\Delta\chi^2/\Delta\text{DOF} = +22.5/+2$, which shows the necessity of this component. Our preferred reflection model results in $\theta_{\text{disk}} = 33^\circ.5^{+20.8}_{-22.4}$ and $a_* = 0.903^{+0.091}_{-0.403}$. The accretion disk inclination is $\sim 10^\circ$

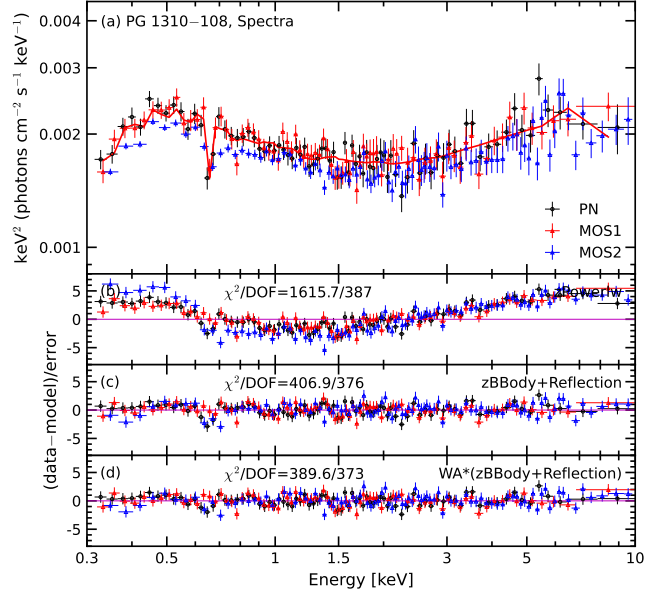


Figure 9. The XMM-Newton and NuSTAR broadband spectral fit of PG 1310–108, showing the best fit with the baseline model (a). All epochs are fit simultaneously. The residuals in terms of error sigmas are plotted for (b) the phenomenological redshifted power-law model, (c) RELXILLCP plus a redshifted blackbody component, and (d) RELXILLCP plus a redshifted blackbody component and a WA. For plotting purposes, the XMM-Newton data have been rebinned to $S/N > 10$.

smaller than the BLR inclination of this source, although lying within the error range. The uncertainties are relatively large because only a single epoch of XMM-Newton observation is available. The lack of higher energy data lost the important information regarding the Compton hump, which is crucial for constraining the reflection fraction, and thus, the systematic errors as well as the statistical errors for the reflection model. Nevertheless, we can obtain an upper limit for the reflection fraction of $R_f = 2.02$, with the 50% value on the MCMC chain equal to $R_f = 0.88$, which implies that $0.88/(1 + 0.88) = 47\%$ of the spectrum arises from reflection. The results from the reflection model should be reasonably reliable. Future observations with broader energy coverage and more (simultaneous) spectral epochs will improve the constraints.

A.6. PG 2209+184

PG 2209+184 was observed by XMM-Newton on 22 November 2017 (0795620201, PI: K. Koljonen; 54.9 ks) and on 30 November 2017, and then again by NuSTAR on 23 November 2017 (60301015002; 101.9 ks). The 22 November observation ended on midnight, only less than 2 hours earlier than the beginning of the NuSTAR observation. Considering that strong variability in X-rays

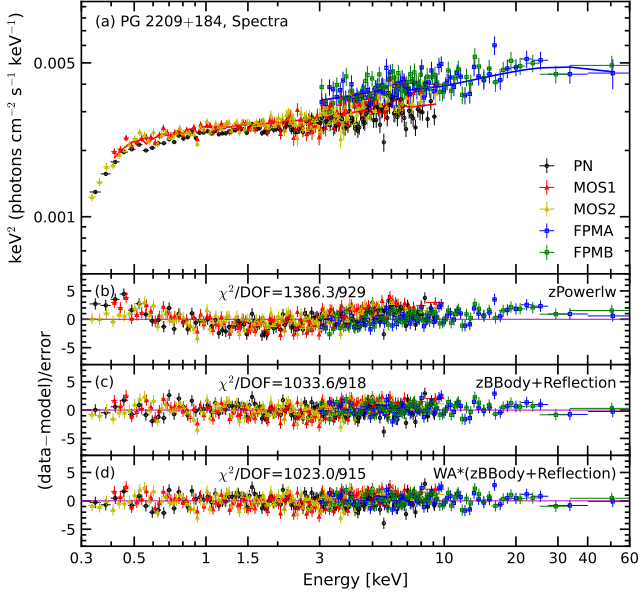


Figure 10. The XMM-Newton and NuSTAR broadband spectral fit of PG 2209+184, showing the best fit with the baseline model (a). All epochs are fit simultaneously. The residuals in terms of error sigmas are plotted for (b) the phenomenological redshifted power-law model, (c) RELXILLCP plus a redshifted blackbody component, and (d) RELXILLCP plus a redshifted blackbody component and a WA. For plotting purposes, data have been rebinned to $S/N > 10$.

has not been reported for this source, we assume the two epochs to be simultaneous and designate them both as epoch *a*. In this case, the corona-related parameters are tied between the two epochs.

As shown in Figure 10, the reflection plus blackbody model improves the power-law fit by $\Delta\chi^2/\Delta\text{DOF} = -352.7/-11$, adding a WA gives $\chi^2/\text{DOF} = 1,023.0/915 = 1.12$ ($\Delta\chi^2/\Delta\text{DOF} = -10.6/-3$), and omitting the blackbody component with $kT = 0.086^{+0.015}_{-0.017}$ keV affects the model by $\Delta\chi^2/\Delta\text{DOF} = +25/+2$. Our reflection modeling results in $\theta_{\text{disk}} = 35.6^{+31.7}_{-25.9}$ and $a_* = 0.989^{+0.009}_{-0.079}$. The constraints are rather loose, even though an epoch of simultaneous data were fit, on account of the low reflection fraction of $0.21 < R_f < 0.72$, for which at most $0.72/(1 + 0.72) = 42\%$ of the spectrum originates from the ionized reflector.

We also test the validity of combining the two observations into one epoch by comparing the results with those from fitting the two observations separately. We untie the corona-related parameters between the two observations and produce the fit and MCMC calculations. In the two-epoch fit, the accretion disk inclination is $\theta_{\text{disk}} = 44.2^{+7.9}_{-4.5}$ and the spin is $a_* = 0.980^{+0.018}_{-0.058}$, which are consistent with the results from the one-

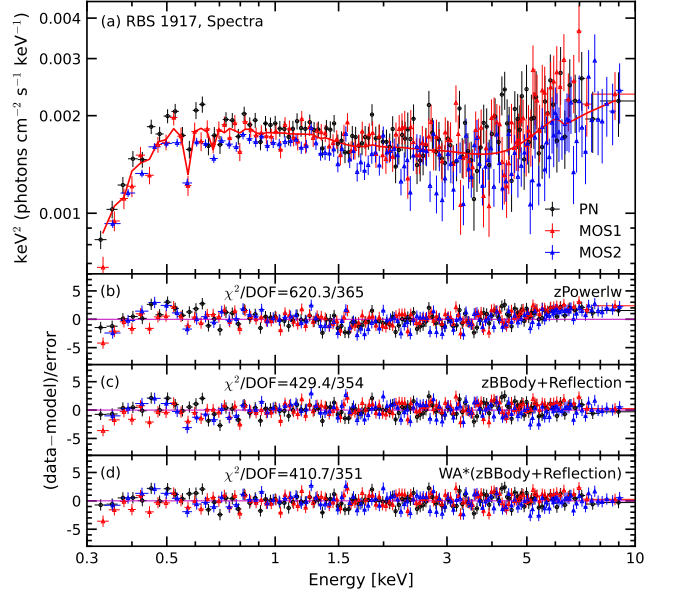


Figure 11. The XMM-Newton and NuSTAR broadband spectral fit of RBS 1917, showing the best fit with the baseline model (a). All epochs are fit simultaneously, and the residuals in terms of error sigmas are plotted for (b) the phenomenological redshifted power-law model, (c) RELXILLCP plus a redshifted blackbody component, and (d) RELXILLCP plus a redshifted blackbody component and a WA.

epoch fit. The reflection fractions for the two epochs are $0.27 < R_f < 0.44$ and $0.10 < R_f < 0.24$, respectively. Their photon indices are exactly the same and equal to the index derived when fit being combined (≈ 1.90), and other parameters are also consistent. These evidence support our choice of combining the two observations into one epoch. However, treating the two observations separately with an additional group of seven free corona-related parameters makes the fit harder to converge, for which a MCMC chain of three times the length of the one-epoch fit is applied here. Moreover, the fit statistic is slightly worse, with $\chi^2/\text{DOF} = 1018.3/908 = 1.121$ comparing to 1.118 from the one-epoch fit ($\Delta\chi^2/\Delta\text{DOF} = -4.7/-7$). The results from the single epoch scenario are thus adopted.

A.7. RBS 1917

RBS 1917 was observed by XMM-Newton twice in 2015. We select the November observation with 35.8ks duration (0762871101, PI: N. Okabe). As with PG 1310–108, the source lacks higher energy observations. The reflection plus blackbody model improves the power-law model by $\Delta\chi^2/\Delta\text{DOF} = -190.9/-11$, whereas including a WA reduces the fit statistic to optimal $\chi^2/\text{DOF} = 410.7/351 = 1.17$ ($\Delta\chi^2/\Delta\text{DOF} = -18.7/-3$) (Figure 11). The blackbody component

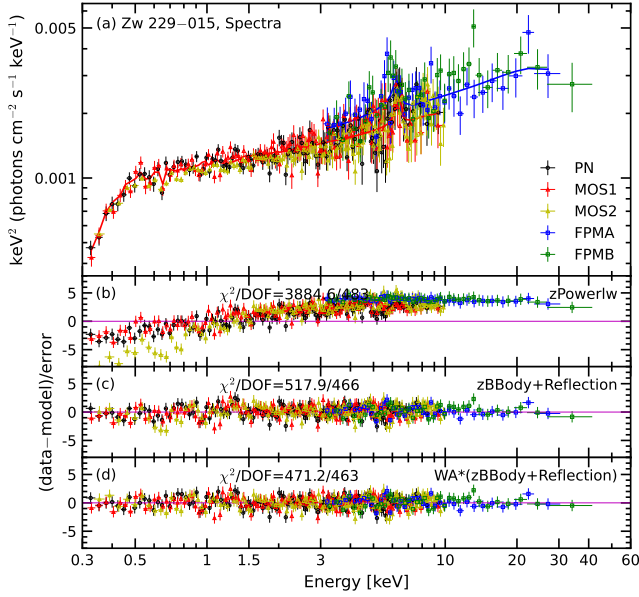


Figure 12. The XMM-Newton and NuSTAR broadband spectral fit of Zw 229–015, showing the best fit with the baseline model (a). All epochs are fit simultaneously. The residuals in terms of error sigmas are plotted for (b) the phenomenological redshifted power-law model, (c) RELXILLCP plus a redshifted blackbody component, and (d) RELXILLCP plus a redshifted blackbody component and a WA.

($kT = 0.248^{+0.009}_{-0.031}$ keV) is necessary because removing it alters the fit by $\Delta\chi^2/\Delta\text{DOF} = +28.3/ + 2$. Our reflection modeling results in $\theta_{\text{disk}} = 17^\circ.2^{+4.5}_{-1.1}$ and $a_* = 0.977^{+0.012}_{-0.003}$. With only one epoch of XMM-Newton data available, the model values, especially those related to broadband or hard X-ray spectral features, are not tightly constrained during the fit. We can derive only rather unlikely lower limits on the reflection fraction ($R_f > 9.87$) and coronal temperature ($kT_e > 380$ keV). Nevertheless, the best-fit inner accretion disk inclination of $\sim 17^\circ$ agrees reasonably closely with the reported BLR inclination of $\sim 20^\circ$.

A.8. Zw 229–015

Zw 229–015 was observed by XMM-Newton in 2011 (0672530301, PI: L. Gallo; epoch *a*, 29.1 ks) and then again by NuSTAR in 2018 (60160705002; epoch *b*). The two observations are not simultaneous, and thus we treat them as separate epochs and use independent corona-related parameters to describe them respectively. As illustrated in Figure 12, the reflection plus blackbody

model improves the power-law model by $\Delta\chi^2/\Delta\text{DOF} = -3,366.7/-17$. Introducing a WA gives a best-fit statistic of $\chi^2/\text{DOF} = 471.2/463 = 1.018$ ($\Delta\chi^2/\Delta\text{DOF} = -46.7/-3$), while removing the blackbody component ($kT = 0.103 \pm 0.001$ keV) degrades the fit by $\Delta\chi^2/\Delta\text{DOF} = +18/+2$. Our reflection modeling indicates $\theta_{\text{disk}} = 26^\circ.2^{+2.5}_{-0.5}$ and $a_* = 0.993^{+0.005}_{-0.059}$.

Adegoke et al. (2017) studied the XMM-Newton spectra and concluded that thermal Comptonization and blurred reflection were equally effective in explaining the data, offering physical insights to the soft excess by comparing the multicolor disk blackbody and smeared wind absorption models. Their Comptonization (COMPTT; Titarchuk 1994) plus redshifted power-law model gave a plasma temperature of 0.632 ± 0.232 keV and $\Gamma = 1.52 \pm 0.10$. Fixing the inclination to 30° , they used reflection calculations of REFLIONX (Ross & Fabian 2005) and the blurring kernel LAOR (Laor 1991) to derive a photon index of $\Gamma = 1.52 \pm 0.082$, which is low compared to our value of $\Gamma \approx 1.8$, and a low iron abundance of $0.469 \pm 0.095 A_\odot$ and yet a high ionization state of $\xi \approx 2300 \text{ erg cm s}^{-1}$. Their fit returned $\chi^2/\text{DOF} = 1436/1404 = 1.023$, which is merely 0.5% bigger than our best-fit model. The discrepancy in the photon index is likely due to the different reflection models used. They also reported the blur index (uniform emissivity index) at 4.22 ± 1.45 that is smaller than both of our indices, and the inner disk radius at 3.999 ± 0.491 that is larger than our value given $a_* = 0.993$. Tripathi et al. (2019) conducted detailed analysis of this source using data from both epochs, as well as additional data from Swift XRT/BAT and Suzaku. They fit the spectra with an ionized partial covering model, RELXILL, and soft Comptonization, respectively, but were also unable to select the best model statistically. They fixed $a_* = 0.998$ and $\theta_{\text{disk}} = 45^\circ$ for the reflection model. In a first attempt with XMM-Newton and Suzaku data, they obtained $\log(\xi/\text{erg cm s}^{-1}) = 2.56 \pm 0.15$ and $R_f \approx 0.4$ with a reduced *C*-stat of $411/355 = 1.16$, parameter values that are consistent with ours. Multi-epoch fits that include NuSTAR data resulted in a reduced *C*-stat of $561/459 = 1.22$ with $\log(\xi/\text{erg cm s}^{-1}) = 2.64^{+0.07}_{-0.17}$. Their photon indices for epoch *a* and *b* are $\Gamma \approx 1.88$ and $\Gamma \approx 1.93$, respectively. Our photon indices are larger than that from Adegoke et al. (2017) by $\Delta\Gamma \approx 0.2$ and smaller than that from Tripathi et al. (2019) by $\Delta\Gamma \approx 0.1$.

REFERENCES

- Adegoke, O., Rakshit, S., & Mukhopadhyay, B. 2017, *MNRAS*, 466, 3951
- Akhila, K., Misra, R., Ezhikode, S. H., et al. 2024, *RAA*, 24, 065025

- Akylas, A., & Georgantopoulos, I. 2021, *A&A*, 655, A60
- Albareti, F. D., Allende Prieto, C., Almeida, A., et al. 2017, *ApJS*, 233, 25
- Antonucci, R. 1993, *ARA&A*, 31, 473
- Arnaud, K. A. 1996, in *ASP Conf. Ser.*, Vol. 101, *Astronomical Data Analysis Software and Systems V*, ed. G. H. Jacoby & J. Barnes (San Francisco, CA: ASP), 17
- Arnaud, K. A. 2016, *HEAD*, 115.02
- Astropy Collaboration, Price-Whelan, A. M., Lim, P. L., et al. 2022, *ApJ*, 935, 167
- Astropy Collaboration, Price-Whelan, A. M., Sipőcz, B. M., et al. 2018, *AJ*, 156, 123
- Astropy Collaboration, Robitaille, T. P., Tollerud, E. J., et al. 2013, *A&A*, 558, A33
- Bahcall, J. N., Kozlovsky, B.-Z., & Salpeter, E. E. 1972, *ApJ*, 171, 467
- Baldwin, J., Ferland, G., Korista, K., et al. 1995, *ApJL*, 455, L119
- Ballantyne, D. R., Sudhakar, V., Fairfax, D., et al. 2024, *MNRAS*, 530, 1603
- Baloković, M., Brightman, M., Harrison, F. A., et al. 2018, *ApJ*, 854, 42
- Bardeen, J. M., & Petterson, J. A. 1975, *ApJL*, 195, L65
- Barth, A. J., Bennert, V. N., Canalizo, G., et al. 2015, *ApJS*, 217, 26
- Barth, A. J., Nguyen, M. L., Malkan, M. A., et al. 2011, *ApJ*, 732, 121
- Barth, A. J., Pancoast, A., Thorman, S. J., et al. 2011, *ApJL*, 743, L4
- Barthelmy, S. D., Barbier, L. M., Cummings, J. R., et al. 2005, *SSRv*, 120, 143
- Baskin, A., & Laor, A. 2018, *MNRAS*, 474, 1970
- Bentz, M. C., Denney, K. D., Grier, C. J., et al. 2013, *ApJ*, 767, 149
- Bentz, M. C., & Katz, S. 2015, *PASP*, 127, 67
- Bentz, M. C., Walsh, J. L., Barth, A. J., et al. 2009, *ApJ*, 705, 199
- Bentz, M. C., Williams, P. R., Street, R., et al. 2021, *ApJ*, 920, 112
- Bentz, M. C., Williams, P. R., & Treu, T. 2022, *ApJ*, 934, 168
- Beuchert, T., Markowitz, A. G., Dauser, T., et al. 2017, *A&A*, 603, A50
- Bevington, P. R. 1969, *Data Reduction and Error Analysis for the Physical Sciences* (New York, NY: McGraw-Hill)
- Blandford, R. D., & McKee, C. F. 1982, *ApJ*, 255, 419
- Boissay, R., Ricci, C., & Paltani, S. 2016, *A&A*, 588, A70
- Bonson, K., & Gallo, L. C. 2016, *MNRAS*, 458, 1927
- Braito, V., Reeves, J. N., Gofford, J., et al. 2014, *ApJ*, 795, 87
- Brewer, B. J., Treu, T., Pancoast, A., et al. 2011, *ApJL*, 733, L33
- Buchner, J., Brightman, M., Nandra, K., et al. 2019, *A&A*, 629, A16
- Burrows, D. N., Hill, J. E., Nousek, J. A., et al. 2005, *SSRv*, 120, 165
- Caballero-García, M. D., Papadakis, I. E., Dovčiak, M., et al. 2020, *MNRAS*, 498, 3184
- Cash, W. 1979, *ApJ*, 228, 939
- Choudhury, K., García, J. A., Steiner, J. F., et al. 2017, *ApJ*, 851, 57
- Collin, S., Kawaguchi, T., Peterson, B. M., et al. 2006, *A&A*, 456, 75
- Costantini, E., Kaastra, J., Korista, K., et al. 2010, *A&A*, 512, A25
- Crummy, J., Fabian, A. C., Gallo, L., et al. 2006, *MNRAS*, 365, 1067
- Czerny, B., Du, P., Wang, J.-M., & Karas, V. 2016, *ApJ*, 832, 15
- Czerny, B., & Hryniewicz, K. 2011, *A&A*, 525, L8
- Czerny, B., Li, Y.-R., Hryniewicz, K., et al. 2017, *ApJ*, 846, 154
- Czerny, B., Różańska, A., & Kuraszkiewicz, J. 2004, *A&A*, 428, 39
- Dauser, T., Garcia, J., Parker, M. L., Fabian, A. C., & Wilms, J. 2014, *MNRAS*, 444, L100
- Dauser, T., Garcia, J., Wilms, J., et al. 2013, *MNRAS*, 430, 1694
- Dauser, T., Svoboda, J., Schartel, N., et al. 2012, *MNRAS*, 422, 1914
- Davis, S. W., & Tchekhovskoy, A. 2020, *ARA&A*, 58, 407
- Deming, W. E. 1943, *Statistical Adjustment of Data* (New York, NY: Wiley)
- Done, C., Davis, S. W., Jin, C., et al. 2012, *MNRAS*, 420, 1848
- den Herder, J. W., Brinkman, A. C., Kahn, S. M., et al. 2001, *A&A*, 365, L7
- Denney, K. D., Peterson, B. M., Pogge, R. W., et al. 2009, *ApJL*, 704, L80
- Denney, K. D., Peterson, B. M., Pogge, R. W., et al. 2010, *ApJ*, 721, 715
- De Rosa, G., Fausnaugh, M. M., Grier, C. J., et al. 2018, *ApJ*, 866, 133
- Ding, Y., Garcia, J. A., Kallman, T. R., et al. 2024, *ApJ*, 974, 280
- Dovčiak, M., Karas, V., & Yaqoob, T. 2004, *ApJS*, 153, 205
- Du, P., Brotherton, M. S., Wang, K., et al. 2018, *ApJ*, 869, 142
- Du, P., Hu, C., Lu, K.-X., et al. 2014, *ApJ*, 782, 45
- Du, P., Hu, C., Lu, K.-X., et al. 2015, *ApJ*, 806, 22

- Du, P., Lu, K.-X., Hu, C., et al. 2016, *ApJ*, 820, 27
- Du, R., Ding, Y., Ho, L. C., & Li, R. 2024, *ApJ*, 963, 152
- Ebrero, J., Costantini, E., Kaastra, J., et al. 2010, *A&A*, 520, A36
- Elitzur, M., & Ho, L. C. 2009, *ApJL*, 701, L91
- Elitzur, M., Ho, L. C., & Trump, J. R. 2014, *MNRAS*, 438, 3340
- Elvis, M. 2000, *ApJ*, 545, 63
- Elvis, M. 2017, *ApJ*, 847, 56
- Emmering, R. T., Blandford, R. D., & Shlosman, I. 1992, *ApJ*, 385, 460
- Eracleous, M., & Halpern, J. P. 1994, *ApJS*, 90, 1
- Esparza-Arredondo, D., Gonzalez-Martín, O., Dultzin, D., et al. 2021, *A&A*, 651, A91
- Esparza-Arredondo, D., Osorio-Clavijo, N., González-Martín, O., et al. 2020, *ApJ*, 905, 29
- Fabian, A. C., Rees, M. J., Stella, L., & White, N. E. 1989, *MNRAS*, 238, 729
- Fabian, A. C., Lohfink, A., Kara, E., et al. 2015, *MNRAS*, 451, 4375
- Fabian, A. C., Zoghbi, A., Ross, R. R., et al. 2009, *Nature*, 459, 540
- Feng, H.-C., Liu, H. T., Bai, J. M., et al. 2021, *ApJ*, 912, 92
- Fischer, T. C., Crenshaw, D. M., Kraemer, S. B., & Schmitt, H. R. 2013, *ApJS*, 209, 1
- Foreman-Mackey, D., Hogg, D. W., Lang, D., & Goodman, J. 2013, *PASP*, 125, 306
- Fouque, P., Durand, N., Bottinelli, L., et al. 1990, *A&AS*, 86, 473
- García, J., Dauser, T., Lohfink, A., et al. 2014, *ApJ*, 782, 76
- García, J., Dauser, T., Reynolds, C. S., et al. 2013, *ApJ*, 768, 146
- García, J. A., Kara, E., Walton, D., et al. 2019, *ApJ*, 871, 88
- Garrett, J. 2021, *SciencePlots (v1.0.9)*, v.1.0.9, Zenodo
- Gehrels, N., Chincarini, G., Giommi, P., et al. 2004, *ApJ*, 611, 1005
- Gerosa, D., Veronesi, B., Lodato, G., et al. 2015, *MNRAS*, 451, 3941
- Ghisellini, G., Padovani, P., Celotti, A., & Maraschi, L. 1993, *ApJ*, 407, 65
- Gianolli, V. E., Bianchi, S., Kammoun, E., et al. 2024, *A&A*, 691, A29
- Gianolli, V. E., Bianchi, S., Petrucci, P.-O., et al. 2024, *Mem. Soc. Astron. Italiana*, 95, 27
- Giovannini, G., Cotton, W. D., Feretti, L., et al. 2001, *ApJ*, 552, 508
- Glozzi, M. & Williams, J. K. 2020, *MNRAS*, 491, 532
- Goodman, J., & Weare, J. 2010, *Communications in Applied Mathematics and Computational Science*, 5, 65
- GRAVITY Collaboration, Amorim, A., Bauböck, M., et al. 2020, *A&A*, 643, A154
- GRAVITY Collaboration, Sturm, E., Dexter, J., et al. 2018, *Nature*, 563, 657
- Grier, C. J., Martini, P., Watson, L. C., et al. 2013, *ApJ*, 773, 90
- Grier, C. J., Pancoast, A., Barth, A. J., et al. 2017, *ApJ*, 849, 146
- Guilbert, P. W., & Rees, M. J. 1988, *MNRAS*, 233, 475
- Guthrie, B. N. G. 1992, *A&AS*, 93, 255
- Haardt, F., & Maraschi, L. 1991, *ApJL*, 380, L51
- Halpern, J. P. 1984, *ApJ*, 281, 90
- Harris, C. R., Millman, K. J., van der Walt, S. J., et al. 2020, *Nature*, 585, 357
- Harrison, F. A., Craig, W. W., Christensen, F. E., et al. 2013, *ApJ*, 770, 103
- Ho, L. C. 2008, *ARA&A*, 46, 475
- Ho, L. C., & Kim, M. 2015, *ApJ*, 809, 123
- Ho, L. C., Rudnick, G., Rix, H.-W., et al. 2000, *ApJ*, 541, 120
- Holmberg, E. 1946, *Meddelanden fran Lunds Astronomiska Observatorium Series II*, 117, 3
- Hopkins, P. F., Hernquist, L., Hayward, C. C., & Narayanan, D. 2012, *MNRAS*, 425, 1121
- Horne, K. 1994, in *ASP Conf. Ser. 69, Reverberation Mapping of the Broad-Line Region in Active Galactic Nuclei*, ed. P. M. Gondhalekar, K. Horne & B. M. Peterson (San Francisco, CA: ASP), 23
- Hubble, E. P. 1926, *ApJ*, 64, 321
- Hunter, J. D. 2007, *Computing in Science and Engineering*, 9, 90
- Igo, Z., Parker, M., Matzeu, G., et al. 2020, *MNRAS*, 493, 1088
- Ingram, A., Ewing, M., Marinucci, A., et al. 2023, *MNRAS*, 525, 5437
- Ingram, A., Mastroserio, G., Dauser, T., et al. 2019, *MNRAS*, 488, 324
- Jansen, F., Lumb, D., Altieri, B., et al. 2001, *A&A*, 365, L1
- Jarrett, T. H., Chester, T., Cutri, R., et al. 2000, *AJ*, 119, 2498
- Jiang, J., Fabian, A. C., Dauser, T., et al. 2019, *MNRAS*, 489, 3436
- Jin, C., Done, C., & Ward, M. 2017, *MNRAS*, 468, 3663
- Jones, D. H., Read, M. A., Saunders, W., et al. 2009, *MNRAS*, 399, 683
- Kalberla, P. M. W., Burton, W. B., Hartmann, D., et al. 2005, *A&A*, 440, 775
- Kammoun, E. S., Nardini, E., & Risaliti, G. 2018, *A&A*, 614, A44

- Kamraj, N., Brightman, M., Harrison, F. A., et al. 2022, *ApJ*, 927, 42
- Kang, J.-L., & Wang, J.-X. 2022, *ApJ*, 929, 141
- Kara, E., Alston, W. N., Fabian, A. C., et al. 2016, *MNRAS*, 462, 511
- King, A. R., Lubow, S. H., Ogilvie, G. I., et al. 2005, *MNRAS*, 363, 49
- Kormendy, J., & Ho, L. C. 2013, *ARA&A*, 51, 511
- Krolik, J. H. 1998, *Active Galactic Nuclei: From the Central Black Hole to the Galactic Environment* (Princeton, NJ: Princeton Univ. Press)
- Krolik, J. H. 2001, *ApJ*, 551, 72
- Laha, S., Reynolds, C. S., Reeves, J., et al. 2021, *Nature Astronomy*, 5, 13
- Laor, A. 1991, *ApJ*, 376, 90
- Levenberg, K. 1944, *Quart. Appl. Math.*, 2, 164
- Li, S.-S., Yang, S., Yang, Z.-X., et al. 2021, *ApJ*, 920, 9
- Li, Y.-R., Songsheng, Y.-Y., Qiu, J., et al. 2018, *ApJ*, 869, 137
- Li, Y.-R., Wang, J.-M., Ho, L. C., et al. 2013, *ApJ*, 779, 110
- Liska, M., Hesp, C., Tchekhovskoy, A., et al. 2021, *MNRAS*, 507, 983
- Lu, K.-X., Huang, Y.-K., Zhang, Z.-X., et al. 2019, *ApJ*, 877, 23
- Magdziarz, P., & Zdziarski, A. A. 1995, *MNRAS*, 273, 837
- Makarov, D., Prugniel, P., Terekhova, N., et al. 2014, *A&A*, 570, A13
- Marconi, A., Axon, D. J., Maiolino, R., et al. 2008, *ApJ*, 678, 693
- Marquardt, D. W. 1963, *J. Soc. Indust. Appl. Math.*, Vol. 11, 2, 431
- Martocchia, A., & Matt, G. 1996, *MNRAS*, 282, L53
- Matt, G., Perola, G. C., & Piro, L. 1991, *A&A*, 247, 25
- Metropolis, N., Rosenbluth, A. W., Rosenbluth, M. N., Teller, A. H., & Teller, E. 1953, *JChPh*, 21, 1087
- Middleton, M. J., Parker, M. L., Reynolds, C. S., et al. 2016, *MNRAS*, 457, 1568
- Miller, J. M., Tomsick, J. A., Bachetti, M., et al. 2015, *ApJL*, 799, L6
- Miniutti, G., & Fabian, A. C. 2004, *MNRAS*, 349, 1435
- Mitsuda, K., Bautz, M., Inoue, H., et al. 2007, *PASJ*, 59, S1
- Mondal, S., Chatterjee, R., Agrawal, V. K., et al. 2024, *PASA*, 41, e072
- Murray, N., & Chiang, J. 1995, *ApJL*, 454, L105
- Murray, N., Chiang, J., Grossman, S. A., et al. 1995, *ApJ*, 451, 498
- Nandra, K., George, I. M., Mushotzky, R. F., et al. 1997, *ApJ*, 477, 602
- Nandra, K., O'Neill, P. M., George, I. M., et al. 2007, *MNRAS*, 382, 194
- Niedźwiecki, A., Szanecki, M., & Zdziarski, A. A. 2019, *MNRAS*, 485, 2942
- Novikov, I. D., & Thorne, K. S. 1973, in *Black Holes (Les Astres Occlus)*, ed. C. DeWitt & B. DeWitt (New York, NY: Gordon and Breach), 343
- Oh, K., Koss, M. J., Ueda, Y., et al. 2022, *ApJS*, 261, 4
- Pancoast, A., Brewer, B. J., & Treu, T. 2011, *ApJ*, 730, 139
- Pancoast, A., Brewer, B. J., & Treu, T. 2014a, *MNRAS*, 445, 3055
- Pancoast, A., Brewer, B. J., Treu, T., et al. 2012, *ApJ*, 754, 49
- Pancoast, A., Brewer, B. J., Treu, T., et al. 2014b, *MNRAS*, 445, 3073
- Pandey, A., Czerny, B., Panda, S., et al. 2023, *A&A*, 680, A102
- Pei, L., Fausnaugh, M. M., Barth, A. J., et al. 2017, *ApJ*, 837, 131
- Peterson, B. M. 1993, *PASP*, 105, 247
- Peterson, B. M. 2006, in *Lecture Notes in Physics* (Vol. 693), *Physics of Active Galactic Nuclei at all Scales*, ed. D. Alloin, R. Johnson, & P. Lira (Berlin and Heidelberg, Germany: Springer), 77
- Petrucchi, P.-O., Gronkiewicz, D., Rozanska, A., et al. 2020, *A&A*, 634, A85
- Petrucchi, P.-O., Ursini, F., De Rosa, A., et al. 2018, *A&A*, 611, A59
- Proust, D., Mazure, A., Vanderriest, C., et al. 1995, *A&AS*, 114, 565
- Quenouille, M. H. 1949, *Annals of Mathematical Statistics*, 20, 355
- Quenouille, M. H. 1956, *Biometrika*, 43, 353
- Reynolds, C. S. 1997, *MNRAS*, 286, 513
- Reynolds, C. S. 2021, *ARA&A*, 59, 117
- Reynolds, C. S., & Begelman, M. C. 1997, *ApJ*, 488, 109
- Reynolds, C. S., Young, A. J., Begelman, M. C., & Fabian, A. C. 1999, *ApJ*, 514, 164
- Ross, R. R., & Fabian, A. C. 2005, *MNRAS*, 358, 211
- Scott, J. E., Kriss, G. A., Lee, J. C., et al. 2004, *ApJS*, 152, 1
- Serafinelli, R., De Rosa, A., Tortosa, A., et al. 2024, *A&A*, 690, A145
- Shakura, N. I., & Sunyaev, R. A. 1973, *A&A*, 24, 337
- Shields, G. A. 1977, *Astrophys. Lett.*, 18, 119
- Skielboe, A., Pancoast, A., Treu, T., et al. 2015, *MNRAS*, 454, 144
- Skrutskie, M. F., Cutri, R. M., Stiening, R., et al. 2006, *AJ*, 131, 1163
- Sokal, A. D. 1996, *Nuclear Physics B Proceedings Supplements*, 47, 172

- Springob, C. M., Haynes, M. P., Giovanelli, R., & Kent, B. R. 2005, *ApJS*, 160, 149
- Steiner, J. F., Narayan, R., McClintock, J. E., et al. 2009, *PASP*, 121, 1279
- Storchi-Bergmann, T., Eracleous, M., Teresa Ruiz, M., et al. 1997, *ApJ*, 489, 87
- Strauss, M. A., & Huchra, J. 1988, *AJ*, 95, 1602
- Strüder, L., Briel, U., Dennerl, K., et al. 2001, *A&A*, 365, L18
- Tagliacozzo, D., Marinucci, A., Ursini, F., et al. 2023, *MNRAS*, 525, 4735
- Titarchuk, L. 1994, *ApJ*, 434, 570
- Tortosa, A., Bianchi, S., Marinucci, A., Matt, G., & Petrucci, P. O. 2018, *A&A*, 614, A37
- Tripathi, S., Waddell, S. G. H., Gallo, L. C., et al. 2019, *MNRAS*, 488, 4831
- Tukey, J.W. 1958, *Annals of Mathematical Statistics*, 29, 614
- Turner, M. J. L., Abbey, A., Arnaud, M., et al. 2001, *A&A*, 365, L27
- U, V., Barth, A. J., Vogler, H. A., et al. 2022, *ApJ*, 925, 52
- Ursini, F., Dovčiak, M., Zhang, W., et al. 2020, *A&A*, 644, A132
- van den Bosch, R. C. E., Gebhardt, K., Gültekin, K., Yildirim, A., & Walsh, J. L. 2015, *ApJS*, 218, 10
- van der Walt, S., Colbert, S. C., & Varoquaux, G. 2011, *Computing in Science and Engineering*, 13, 22
- Vasudevan, R. V., Brandt, W. N., Mushotzky, R. F., et al. 2013, *ApJ*, 763, 111
- Vestergaard, M., & Peterson, B. M. 2006, *ApJ*, 641, 689
- Villafañá, L., Williams, P. R., Treu, T., et al. 2022, *ApJ*, 930, 52
- Villafañá, L., Williams, P. R., Treu, T., et al. 2023, *ApJ*, 948, 95
- Wada, K. 2012, *ApJ*, 758, 66
- Waddell, S. G. H., & Gallo, L. C. 2020, *MNRAS*, 498, 5207
- Wang, J.-M., Du, P., Hu, C., et al. 2014, *ApJ*, 793, 108
- Weisskopf, M. C., Soffitta, P., Baldini, L., et al. 2022, *Journal of Astronomical Telescopes, Instruments, and Systems*, 8, 026002
- Wilkins, D. R., & Fabian, A. C. 2011, *MNRAS*, 414, 1269
- Williams, P. R., Pancoast, A., Treu, T., et al. 2018, *ApJ*, 866, 75
- Williams, P. R., Pancoast, A., Treu, T., et al. 2020, *ApJ*, 902, 74
- Wills, B. J., & Brotherton, M. S. 1995, *ApJL*, 448, L81
- Wilms, J., Allen, A., & McCray, R. 2000, *ApJ*, 542, 914
- Winter, L. M., Mushotzky, R. F., Tueller, J., et al. 2008, *ApJ*, 674, 686
- Wu, Z., Ho, L. C., & Zhuang, M.-Y. 2022, *ApJ*, 941, 95
- Xiao, M., Du, P., Horne, K., et al. 2018, *ApJ*, 864, 109
- Xiang, X., Ballantyne, D. R., Bianchi, S., et al. 2022, *MNRAS*, 515, 353
- Yaqoob, T., & Padmanabhan, U. 2004, *ApJ*, 604, 63
- Yu, N., Ho, L. C., & Wang, J. 2020, *ApJ*, 898, 102
- Zdziarski, A. A., Johnson, W. N., & Magdziarz, P. 1996, *MNRAS*, 283, 193
- Zdziarski, A. A., Szanecki, M., Poutanen, J., et al. 2020, *MNRAS*, 492, 5234
- Zheng, X. C., Zhang, Y., & Röttgering, H. J. A. 2024, *A&A*, 686, A169
- Zhuang, M.-Y., Ho, L. C., & Shangguan, J. 2018, *ApJ*, 862, 118
- Życki, P. T., Done, C., & Smith, D. A. 1999, *MNRAS*, 309, 561